Experimental Thermal and Fluid Science 159 (2024) 111272

Contents lists available at ScienceDirect

Experimental Thermal and Fluid Science

journal homepage: www.elsevier.com/locate/etfs

A new methodology for experimental analysis of single-cavity bubble's nucleation, growth and detachment in saturated HFE-7100

Ivan Talão Martins [a], Pablo Fariñas Alvariño [b,*], Luben Cabezas-Gómez [a]

[a] Department of Mechanical Engineering, Heat Transfer Research Group, São Carlos School of Engineering (EESC), University of São Paulo (USP), São Carlos 13566-590, Brazil

[b] Universidade da Coruña, Campus Industrial de Ferrol, Ferrol, 15403, A Coruña, Spain

ARTICLE INFO

Keywords:
Experimental bubble growth
Image processing
Ensemble averaging

ABSTRACT

The study of single bubble nucleation, growth and detachment processes has being carried out with remarkable relevance in the last fifty years. The complexity of the associated phenomena are still a challenge for the researchers in the field, yielding a lot of works trying to explain the enrolled mechanisms. These studies include experimental, numerical and even theoretical approaches. In particular but not exclusively for numerical approaches, it is of essential importance having a solid and detailed experimental description of the full event. It is in this context that this work emerges, proposing a methodology for characterizing the single bubble nucleation, growth and detachment process. This methodology is based in the determination of a "typical bubble" that represents the whole phenomena, providing the reconstruction of a main bubble life-cycle with its uncertainty (both in space and time). This reconstruction allows the determination of several important characteristics, such as bubble volume, apparent contact angle, dry radius, and the forces acting on the bubble. This work analyzes a set of bubbles growing from a cavity of 91 μm diameter, under saturated conditions at 0,583 bar and superheating of 25,8 °C. All the outputs were obtained considering a carefully uncertainty determination and propagation from both systematic and random sources, which are not negligible as it is demonstrated in this work. The importance of considering a sufficient number of bubbles to characterize the phenomenon was also addressed, considering an analysis of uncertainties for different set of bubbles. The methodology was also confronted to previous approaches reported elsewhere, that ensured its performance, robustness, and validation.

1. Introduction

Studies on nucleate boiling took advantage of image analysis throughout more than 55 years [1]. Photographic reports were originally intended to develop analytical models on prediction of bubble growth parameters, such as growth rate [2], detachment size and frequency [3–5], or any other characteristic feature of bubbles structure. Nowadays, these experimental results are still of utmost importance [6], since the coupled momentum–energy problem is not solved yet [7].

Advent of numerical methods on nucleate boiling requires experimental evidence to compare with. For example, the numerical exercises developed by [8,9] proved the importance of experimental data for validating the numerical methods. Regretfully, past experimental studies published results that scarcely report the bubble dynamics parameters in a detailed manner. Indeed, the scarce photographic galleries yielding detailed experimental results are heavily referenced [10], and constitute an active area of research [11], because their results are widely used to compare with numerical results.

Recall that pool boiling encompasses a set of complex phenomena that produce a countless number of possible instances of bubble growth. As a result, the whole problem constitutes a challenging task for numerical methods and, therefore, simplified experimental studies considering adiabatic bubbles of non-condensable gases [12] yield useful data to compare with. Di Bari and Robinson [12] studied the bubbles growth with air injected through calibrated orifices at given mass flow rates from the bottom of a chamber of water. Their results were quite interesting, since forces, contact angle, and some profiles of the bubbles were reported. However, the bubble growth rate is determined by the mass flow rate of the needle and, in addition, no information was reported on how many bubbles were considered for their reports. This last issue is of utmost importance for thermally

* Corresponding author.
E-mail addresses: ivanmartins@usp.br (I.T. Martins), pablo.farinas@udc.es (P. Fariñas Alvariño), lubencg@sc.usp.br (L. Cabezas-Gómez).

https://doi.org/10.1016/j.expthermflusci.2024.111272
Received 1 January 2024; Received in revised form 14 June 2024; Accepted 17 July 2024
Available online 26 July 2024

Nomenclature

Acronyms

SF	Scaling factor of the taken video frames [mm/px]
FFT	Fast Fourier Transform
fps	Frames per second taken by the fast camera
px	Each of the pixels in the picture taken by the fast camera
RTD	Resistance Temperature Detector

Greek Symbols

α	Scale factor for weight calculation in the Gaussian filter[–]
ΔT	Temperature difference [°C]
ϵ_t	Elemental time to define the displacement of W curves [s]
ϕ	Dynamic contact angle [deg]
ρ	Density [kg/m^3]
σ	Standard deviation for Gaussian filter [–]
τ	Time displacement, auxiliary variable [s]
$\tilde{W}(y,t)$	Width of the average bubble as function of time and high over the nucleation site in [mm], for its relationship is provided by SF
ς	Surface tension [kg/s^2]
t	Time [s]
$W(y,t)$	Width of each single bubble as function of time and high over the nucleation site [mm]
$w(y,t)$	Width of each single bubble as function of time and high over the nucleation site [px]
y	Vertical distance from any point to the nucleation site in [px] or [mm], for its relationship is provided by SF

Roman Symbols

$\forall$	Volume of the bubble [mm^3]
$\mathbb{P}$	Pressure [bar]
$\mathbf{g}$	Gravity acceleration
B	Total number of bubbles recorded in the video
D	Average difference between curves in [mm]
F_b	Buoyancy force [N]
F_L	Lift force [N]
F_ς	Surface tension force [N]
F_{cp}	Contact pressure force [N]
F_{uy}	Unsteady growth force [N]
H	Distance between the center of consecutive bubbles [m]
I	Intensity of pixel, so that $0 \leq I \leq 255$
m	A positive integer [–]
n	A positive integer [–]
N_x	Total number of pixels of the region of interest along the horizontal direction [px]
N_y	Total number of pixels of the region of interest along the vertical direction [px]
P	Number of points, or events, to define the average width, $\tilde{W}$, of the bubble [–]
p	Each point, or event, that defines the average width, $\tilde{W}$, of the bubble [–]
R	Radius [mm]
R_r	Equivalent radius at the top of the bubble [m]
S_a	Roughness average [μm]
S_q	Root mean square roughness average [μm]
T	Temperature [°C]
u	Uncertainty [$Givenmagnitude$]
v	Velocity [m/s]

Subscripts/superscripts

$\tilde{W}$	Related to average width of the bubble
$apex$	At the apex of the bubble
b	Related to a particular given bubble
$Clos$	Value after the closing morphological transformation
d	Dry, in contact with vapor phase
eq	Equivalent to spherical radius
$GaussBlur$	Value after the Gaussian filter is applied
l	Related to liquid phase
ll	Stands for a lower limit
max	Makes reference to the maximum of a given variable
min	Makes reference to the minimum of a given variable
$nvtl$	At the near vicinity of the triple line, within the bubble interphase
ref	Stands for the bubble with the largest period at each vertical distance from the nucleation site
sat	Under saturated condition
t	Related to time
tl	At the triple line
ul	Stands for an upper limit
v	Related to vapor phase
$wall$	At the heated wall

driven growth of bubbles, since natural convection on the hot surface is commonly necessary, and it brings forth a sort of stochastic bubble growth. This last statement will be clearly illustrated in this manuscript.

Thermal growth of a bubble in an infinite superheated liquid is already solved by Avdeev [7]. However, bubble growth from an active cavity at a heated wall encompasses other phenomena that need additional research effort. Chen et al. [13] studied the evolution of the microlayer of water bubbles through laser interferometry. They [13] also reported a photographic gallery with the evolution of a bubble shape for heat flux $q'' = 80$ kW/cm^2. However, this excellent contribution [13] was focused on the microlayer geometry, and did not report the time evolution of the whole bubble.

Jung and Kim [14] measured the dynamic and thermal evolution of a bubble immersed in water under atmospheric pressure. They [14] applied the technique of laser interferometry to address both the geometry of the microlayer, and split its contribution on the global heat transfer. They also reported the roughness of the hot surface (ITO) and its corresponding static contact angle, which is of paramount importance for numerical simulations, even though these parameters are scarcely reported in other references. Jung and Kim [14] developed an outstanding report of results: It encompassed the time evolution of the apparent contact angle and the corresponding shape of the bubble. One of their interesting conclusions was that microlayer is responsible for 17% of the total heat transfer throughout the bubble life-cycle. Therefore, it is also interesting pay attention to other mechanisms, which are responsible for majority of heat transfer. As a last remark, it is interesting to note that [14] did only studied one single bubble and, therefore, random uncertainty could not be addressed.

Hubert et al. [15] developed a DNS study on the growth of a water bubble. Their work was mainly focused on the microregion, which is the inner part of the microlayer, or the close vicinity of the true contact line. The model of the microregion is an open issue on nucleate boiling [15]. These authors illustrate a relation between the apparent macroscopic contact angle and the microscopic contact angle at the contact line. Therefore, experimental evidence on the apparent contact angle is necessary to properly address the microregion models. As usually, their numerical results are confronted with equivalent radius evolution and detachment radius alone.

Some other references reported the experimental growth of a single bubble at a heated wall, see for instance [11,16,17]. All of them follow the same approach: a fast camera records the bubble growth and report both the operating conditions and geometrical features. The work of Michaie et al. [17] is a significant reference on identifying and reporting the bubble profile, growth period, and, when possible, the corresponding uncertainties. In this regard, note that they [17] illustrate their difficulties on yielding the waiting time since they found "largely scattered" values. They also report the bubble departure frequency for a small set of bubbles, even though they admit their data is scarce. Indeed, for the lowest pressure they yielded a departure frequency uncertainty about 100% (see Fig. 8 in [17]). As a result, more research is needed on this regard, not only for yielding additional experimental data, but also to propose new methodologies to overcome these difficulties.

Recently, two interesting publications by Mahmoud and Karayiannis [18,19] addressed in a very detailed way a bubble growth on a smooth heated surface of copper, considering deionized saturated water under pool boiling conditions at atmospheric and sub-atmospheric pressures. The authors presented detailed experimental measurements obtained with a high-speed, high-resolution camera with a microscopic lens. They provided a thorough discussion on the measurement and analysis of bubble dynamics parameters. They also studied the bubble growth process using models for homogeneous and heterogeneous boiling. The analytical and numerical results were compared with the experimental ones, establishing several important conclusions and making clear the necessity of more experimental researches with different fluids [19]. In this paper the authors also provided evidence of the existence of large variation from cycle to cycle of the bubble growth and departure diameter. These findings can be considered a strong justification to the development and use of the methodology proposed in this paper.

This manuscript will propose a new procedure to analyze a bubble growth and its detachment. Our proposed procedure will be based on identification of the bubble contour for each taken frame. The watershed transformation [20,21] is a well established method for this task. However, as denoted by [22–24] this procedure must be carefully applied because the excess of noise capturing can cause an over-segmentation, which can hinder contour identification. Thus, instead of the traditional one, a marker-based watershed segmentation [25] is implemented after applying a noise-removal pre-processing, which helps to avoid the over-segmentation and allows a more precise capturing of the bubble boundary [26].

The proposed methodology for the bubble capture must also be validated. Regretfully, the authors could not find previous available references containing videos as supplementary information reporting the corresponding bubble shape, its equivalent volume, or any other feature. As a result, this new procedure was validated using available data from Siedel, Cioulachtjian and Bonjour [16], through their yielded array of pictures and their corresponding reported volume. This benchmark exercise is reported in Appendix B, where the resulting volume is shown to fall within the uncertainty region.

Given that bubble growth is a periodic phenomenon, it is expected that bubble's features behave under some periodic pattern. Thus, a rigorous frequency analysis through Fast Fourier Transform (FFT) will be carried out to determine the nucleation period. The results are compared with the traditional method based on measuring the whole period of one single bubble.

This research will also show an additional check on the characteristic bubble regarding its volume growth with time. Note that several correlations can be found in the literature and, therefore, it is interesting to evaluate how far these correlations are in comparison to the data yielded herein. We will consider correlations for bubble growth both in a superheated liquid, as well as for bubbles nucleation at an active cavity. The comparison will illustrate a wide dispersion between available correlations, as well as the convenience of further experimental evidence.

We will also prove that a small number of bubbles does not suffice to characterize the most plausible bubble under a given set of operating conditions. A rigorous assessment of the bubble shape uncertainty was necessary to pose previous statement. Random uncertainty cannot be disregarded for it is the stronger one. To a best knowledge of the authors, there is no one single approach reporting the random uncertainty of bubble shape in a rigorous manner. Note, in addition, this manuscript will be released with a table of supplementary information reporting the average bubble shape. Expectedly, this supplementary information will be useful to compare with numerical results reported elsewhere. Both the bubble shape and its uncertainty are reported with complete resolution in time-space domains, according to our experimental setup capabilities.

2. Experimental procedure

In this section we are presenting the boiling facility employed in the experimental campaign for performing the experiments and required measurements (Section 2.1), as well as the conventional image treatment (Section 2.2), that was developed prior to apply our proposed methodology (Section 3)

2.1. Experimental setup

The components of the boiling vessel, as well as the those of the measuring system, are described in [27]. Thus, this section will report all relevant data regarding the test section, fluid, video system, and operating conditions.

The test section is shown in Fig. 1(a), and was machined from a copper (Cu-Electrolytic Tough Pitch R300 – Cu> 99,9%) rod. Its thermal conductivity was experimentally yielded and is reported in Fig. 2.[1] Four T type thermocouples yield the temperature at the central axis of the test section shown in Fig. 1(a). The first one was 8.9 mm from the heated surface, and the other three are spaced 5 mm from each other. The Fourier law provides both the temperature at the heated wall, and the applied heat flux, according to the yielded temperatures and the thermal conductivity reported in Fig. 2.

The heated surface in contact with the fluid in the boiling vessel is a 30 mm diameter circle. The hot surface was polished with a Struers-Labopol facility. The last sandpaper was a silicon carbide P500 foil. Afterwards, the polishing procedure was concluded with a suspension of 1 μm diamond particles. Fig. 1(c) shows the heated surface texture, whose roughness parameters were $S_a = 0.024 \pm 0.005$ μm and $S_q = 0.033 \pm 0.006$ μm. The roughness parameters were determined taking five topographies in different positions along the surface, to ensure its homogeneity throughout the heated surface. We intend to attain the smallest possible surface roughness for discarding its potential effect on the bubble nucleation.

Four single-cavities were crafted in a straight line, while other four double-cavities were made in a second straight line right above the

[1] The thermal conductivity of the test section was provided by a Physical Property Measurement System (PPMS) 9T from the company Quantum Design at the University of Zaragoza-Spain.

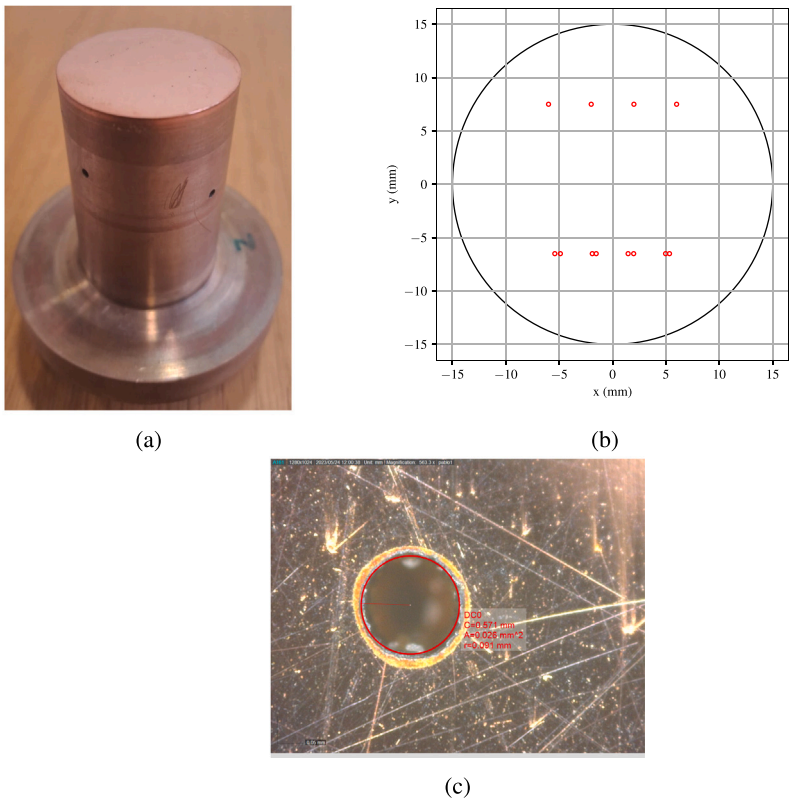

Fig. 1. (a) Test section. (b) Illustration of the nucleation sites made in the test section (c) Nucleation site.

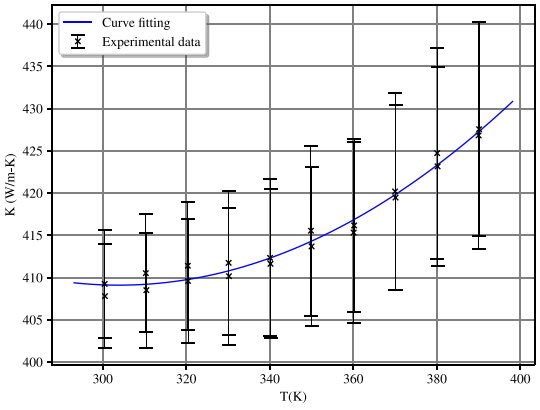

Fig. 2. Copper conductivity.

first one. An illustration of the cavities can be seen in Fig. 1(b). They were made by a femtosecond laser facility SPIRIT 1040-4 from the company Spectra-Physics. The wavelength of the laser was 1040 nm with pulses of 390 fs. The diameter of these cavities are about 91 μm, and the laser pulses were applied up to the laser limit for the ablation procedure, where the laser becomes unable to remove more material from the cavity. A top-visualization of these round cavities are depicted in Fig. 1(c), where the diameter of one cavity is shown. The active nucleation site was recorded with a microscope of the company Dino-Lite with a RK-10-PX mounting device.

Prior to enter the fluid, HFE-7100, into the boiling vessel, a vacuum pump (Telstar model 2F) removed the air inside the chamber. Thereafter, the fluid was degassed through continuously boiling at a pressure slightly above atmospheric. Two precision RTDs, one inserted in the liquid phase and the other into the vapor phase, yield the temperature difference between both phases. Degassing process finished when the temperature difference falls below 0.05K. Therefore, the experiments took place under saturated conditions.

The boiling chamber (see Fig. 3) is a stainless-steel vessel with two opposed windows. Both windows are circular and were designed to observe the heated surface horizontally, from the level where the window attains its maximum diameter. A JUMO pressure transducer located at the top of the boiling vessel, with an operating range from 0 to 2500 kPa, and an uncertainty of 0.01 Bar, yields the pressure inside the boiling chamber. Besides, two precision Pt100 probes measured both liquid and vapor temperatures, to check that HFE-7100 fluid is operated under a saturated condition. Four T type thermocouples were used to determine the temperature at the boiling surface. The thermocouples were inserted in the test section (see Fig. 1(a)) into four 1 mm diameter holes, 5 mm apart from each other. All details in terms of temperature uncertainty propagation can be found in [27]. The light source was in the rear window and was constituted by a 117 W non-pulsed led lamp to avoid contrast fluctuations in high-speed videos. The lamp dimension fits the window clearance diameter, which in addition was covered by a translucent film to enhance light diffusion. Videos were taken with a high-speed camera model Mini UX-50 from the company Photron at 4000 frames per second (fps). The camera was operated with a 150 mm macro lens from Sigma company. The spatial resolution of video was 1280 px times 512 px.

The pressure in the boiling vessel was $\mathbb{P}_{sat} = 0,583$ bar, and the wall superheating was $\Delta T = T_{wall} - T_{sat} = 25.80 \pm 0.30$ °C. We have chosen this saturation pressure to ensure that the algorithm works properly for non-conventional bubbles, even in terms of the yielded uncertainty.

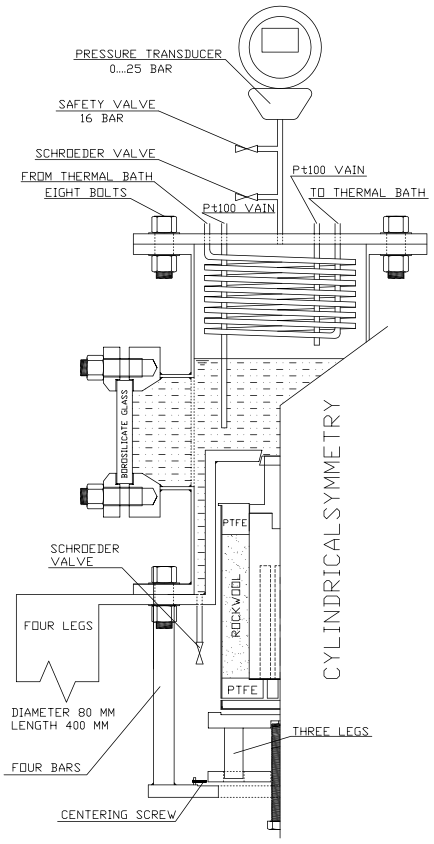

Fig. 3. General arrangement of the experimental rig.

2.2. Bubble contour capturing

This section will report the methodology to capture the bubble contour, which are based on traditional procedures that are easily found in open literature, with the use of Python language. Therefore, this section provides the aggregated procedures applied to the taken video, in order to ensure the whole process repeatability elsewhere.

The procedure starts by desegregating the video into its complete set of frames. The "region of interest" is defined as the portion of the picture where the bubble grows and detach the heated surface. The region of interest is kept for all frames throughout the time-span of the video. Thus, the area of the pictures outside the region of interest was disregarded since, eventually, it does not contain useful information. In addition, treating the region of interest alone made the ongoing algorithm more computationally tractable.

The lowermost border of the region of interest must be located at the level of the nucleation site. Note that this position is kept throughout the whole video. The footprint of the nucleation site is clearly observable throughout the bubble waiting time, though it was not shown herein for the sake of brevity. Identification of this border is also supported by the reflection of the bubble on the heated surface, given its mirrored finish. Thus, determining the lowermost border of the region of interest was a hand-made procedure. The uppermost limit of the region of interest was defined high enough to capture entire bubbles after their detachment, but keeping a clear background all around the bubble to allow the contour identification. The lateral extent of the region of interest is also defined large enough to capture entire bubbles. A bubble sample with its corresponding region of interest is shown in Fig. 4. Note that x and y axis denotes the dimensions within the region of interest, in px, for width and height, respectively. The resolution of the region of interest in pixels is $\left(N_x, N_y\right) = (300, 210)$.

The procedure goes on with the application of a Gaussian filter to the region of interest. This step reduces the noise and the effects of light refraction, helping in the contour identification process. The filter blurs the image, substituting each pixel intensity by the weighted average from the considered neighbor pixels. The number of neighbor pixels is defined by the kernel size: a matrix $k = [n, m]$ where n is the number of pixels in x direction and m, in y direction, centered at the pixel in which value will be replaced. The weights are defined by a 2D Gaussian function with standard deviation σ (see Eq. (1)), representing how strong is the neighbor pixels' influence in the center pixel's intensity. As the scale factor α is selected in such a way that $\sum_{ij} G_{ij} = 1$, the final intensity of each pixel is given by $I^{GaussBlur}(x, y) = \sum_{ij} G_{ij} I(x_i, y_j)$, with $i = 0, \ldots, n-1$ and $j = 0, \ldots, m-1$ [28]. The positions x and y are given in pixels, with $x_i = x + \left[i - (n-1)/2\right]$ and $y_j = y + \left[j - (m-1)/2\right]$. In this paper, the chosen kernel for the Gaussian filter was $k = [5, 5]$ px, with a standard deviation about $\sigma = 1.10$.

$$G_{ij} = \alpha e^{-\frac{\left[(x_i - x)^2 + (y_i - y)^2\right]}{2\sigma^2}} \tag{1}$$

The next step is the inverse Otsu's binarization [29]. This procedure re-assigns the intensity of each pixel within the region of interest according to a threshold value. Then, any pixel intensity above this value is re-assigned to 255 (white), whereas the rest of pixels' intensity was set to 0 (black). The Otsu's algorithm is responsible for finding an optimum threshold value, which was initially set as 5.10 in this work. The inverse binarization is considered in furtherance of identifying the main object of interest (the bubble) as white instead of black, which helps the identification of background and foreground regions in the marker-based segmentation.

The next pre-processing step is the noise removal by a closing morphological transformation. It consists in a dilation of the white pixels, followed by an erosion of the image [30,31], which can remove small spots (eventual noise) preserving the shape of big objects, such as the bubble. The dilation process changes the pixel intensity by the maximum value found in a neighborhood, determined again by the kernel. In contrast, the erosion changes it by the minimum intensity of the neighborhood. Mathematically, both processes can be translated to $I^{dilat}(x, y) = max_{ij}^{(x_i, y_j) \neq (x, y)} \left\{ I(x_i, y_j) \right\}$ and $I^{eros}(x, y) = min_{ij}^{(x_i, y_j) \neq (x, y)} \left\{ I(x_i, y_j) \right\}$. Consequently, the entire closing transformation is represented by:

$$I^{clos}(x, y) = \text{eros}\left\{\text{dilat}\left\{I(x, y)\right\}\right\} = min_{ij}^{(x_i, y_j) \neq (x, y)} \times \left\{ max_{ij}^{(x_i, y_j) \neq (x, y)} \left\{ I(x_i, y_j) \right\} \right\}, \tag{2}$$

Recall that $x_i = x + \left[i - (n-1)/2\right]$ and $y_j = y + \left[j - (m-1)/2\right]$, with $i = 0, \ldots, n-1$ and $j = 0, \ldots, m-1$, being $k = [n, m]$ the kernel. In this case, it was considered $k = [3, 3]$ px, performing 3 iterations, which means that the closing transformation was applied three consecutive times. Fig. 5 depicts the effects of these three steps (Gaussian blur, Otsu's binarization, and morphological transformation) for the bubble shown in Fig. 4.

In the sequence, the marker-based watershed segmentation is finally applied in order to identify the contour of the bubbles. The procedure starts with the identification of regions that are "sure background" and "sure foreground". The watershed segmentation will be only applied over the "unknown" region, which is the remaining portion of the region of interest, once the sure background and sure foreground are removed.

For the sure background identification, a dilation with a 3 × 3 px kernel is performed considering 5 iterations. As the white shapes are expanded in this procedure, the contour positions are included and the remaining part of the figure is composed by just background shapes.

For the sure foreground, it would be reasonable the application of an erosion process that removes the boundary pixels and retract the objects. However, since there is the possibility of having objects connected, two bubbles merging for example, the erosion may not be

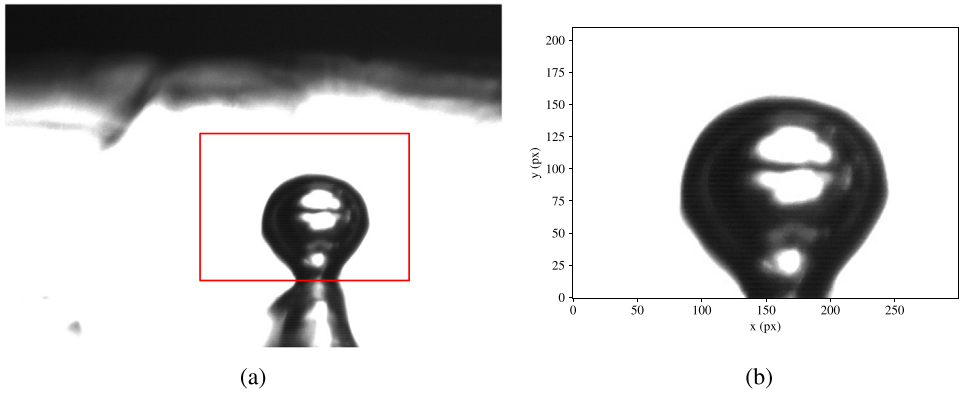

Fig. 4. (a) Frame of the recorded video. (b) Region of interest from the original frame.

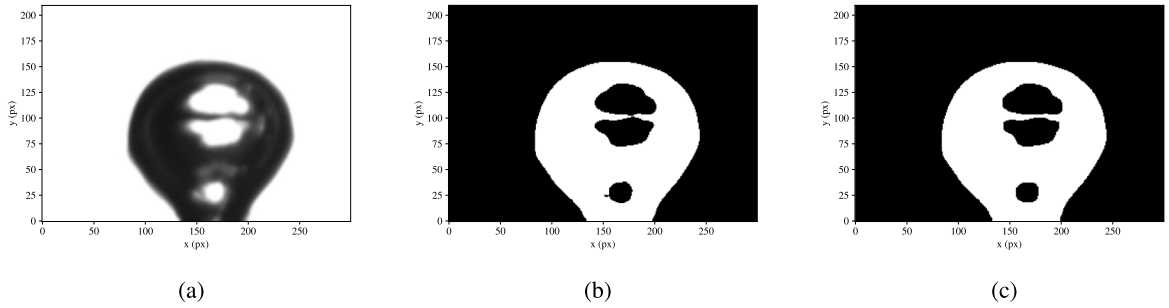

Fig. 5. (a) Result after the Gaussian blur filter. (b) Threshold image by Otsu's binarization. (c) Result after the morphological transformation of closing.

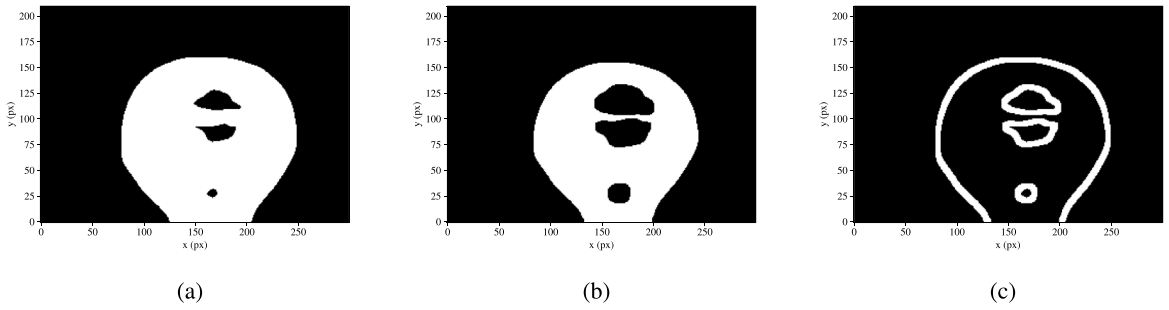

Fig. 6. (a) Sure background. (b) Sure foreground. (c) Unknown region (in white), where it is applied the watershed segmentation.

the best choice for finding the sure foreground area. Alternatively, it is applied a distance transformation (it is considered the Euclidean distance with a 3 × 3 mask) that returns for each pixel location the distance to the nearest background pixel. Next, a threshold is applied in the previous output, transforming every pixel with a distance less than 2% of the maximum distance found in a background pixel (black). This procedure removes boundary pixels without additional issues related to connected objects.

At last, the unknown region consists in the remaining area that are not foreground neither background (see Fig. 6).

The bubble contour capturing procedure for each frame can be summarized in the following steps:

1. Cut the figures in the region of interest, discharging the rest;
2. Apply Gaussian blur filter;
3. Apply inverse Otsu's binarization as a first segmentation;
4. Remove noise by closing morphological transformation;
5. Begin the marker-based watershed segmentation:
   (a) Find sure background by dilation;
   (b) Find sure foreground by distance transformation followed by threshold;
   (c) Find the unknown region subtracting the sure foreground of the sure background;
   (d) Apply watershed only in the unknown region for identifying the contours;

This stage finishes with the scaling between number of pixels and true distance in previous figures. Given that distance between consecutive potential sites is already known, it was necessary to record, at least, two potentially active sites for calibration purposes. Assuming a measurement uncertainty about 2 px for each nucleation site position, the number of pixels between two consecutive nucleation sites was

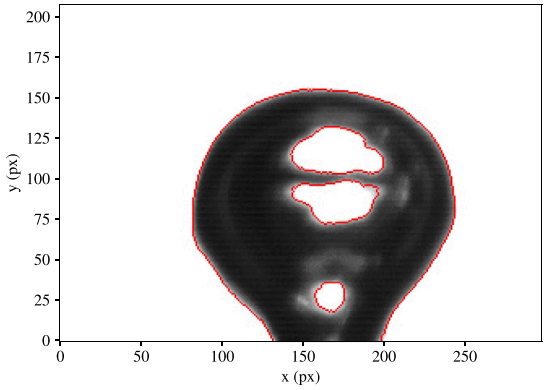

Fig. 7. Result of the image segmentation procedure, and the corresponding assessment with the original frame reported in Fig. 4(b).

401 ± 3 px. Note the reference distance chosen for calibration, 401 px, is well beyond the typical size of the bubble detachment width, ≈180 px, see Fig. 7. The true distance between two nucleation sites was yielded by the positioning tool of the femto-second laser, and was set to 3.433 ± 0.001 mm. Thus, the procedure provides both the scale factor of the pixels, and its corresponding systematic uncertainty, $SF = 8.56 \cdot 10^{-3} \pm 0.06 \cdot 10^{-3}$ mm/px. As a reference, recall that bubble detachment maximum width was ≈180 px. Given the yielded scale factor, this maximum width corresponds to $\approx 1,54 \pm 0,18$ mm. Recall it stands for the systematic uncertainty alone, which will be eventually negligible. None has been posed yet on the random uncertainty that will be addressed in the next section.

Beyond the systematic uncertainty from the scale factor determination, the watershed procedure for itself has also some uncertainty associated to the bubble contour captured and its real position. This fact can be better perceived in Fig. 7 and its reason can be related both with the precision of the segmentation method, which has limitations, and with the effects of light diffraction by the hot fluid in movement surrounding the bubble. In this way, some uncertainty must be considered to represent the precision in the capture of the bubble's contour, in addition to the uncertainty of the scale, previously mentioned. In this work, the value assumed was about 4 px, which seems to be a reasonable choice, given the image segmentation results reported in Fig. 7.

The consideration of these uncertainties (from scaling and from watershed segmentation) for the width scaling operation and for the mean bubble characterization follow the error propagation criteria for uncorrelated quantities. See Appendix A for details.

3. Methodology and results

In Section 3.1 we introduce the new methodology developed by the authors for the characterization of the typical bubble from a set of bubbles. It is important to effort that the procedure presented in Section 2.2 for image analysis is of great importance for allowing the application of the new procedure, which needs the data information about the bubbles' width with time (t) and space (y). In Section 3.2 we provide an additional insight on physical aspects inherited from yielded data.

3.1. Methodology for the characterization of the typical bubble

Note that the bubble shape in Fig. 7 is not symmetric. However, symmetry is an expected feature for a single ideal bubble. Indeed, the shape shown in Fig. 7 is a single realization (an instance) of an existing bubble that, for sure, will never take place again. Previous statements are somehow supported by Michaie et al. [17] regarding the waiting time and departure frequency. They [17] stated "...large scattering could be explained by the fact that the liquid movements provoked by the departure of the former bubble and its condensation are of a stochastic nature...". As a result, experimental random uncertainty seems to be relevant and unavoidable. It will be necessary a large enough amount of bubbles for addressing the random uncertainty. This section will provide a methodology to determine (i) the most probable contour evolution of a bubble (ii) the random plus systematic uncertainty for the contours of the typical bubble and (iii) the minimum number of bubbles that suffices to characterize previous data. As already stated, these kind of data cannot be easily found in scientific repositories, even though it constitutes so relevant data for numerical comparison purposes and assessment of analytical models.

Recall that segmentation from previous section provided the bubble width, W [mm] or w [px], at any distance above the nucleation site, y, and time, t. Recall that magnitudes W and w might be used interchangeably, for $W = wSF$. Therefore, the function $W(y,t)$ is already known. A conventional sketch of the captured bubble width is shown in Fig. 8(a). This figure reports the width, w, of the bubble that took place at $t = 8.75$ ms as a function of the vertical distance to the nucleation site, y. The generalization of Fig. 8(a) is reported in Fig. 8(b), where the function $W(y,t)$ is shown. For ease of observation, Fig. 8(b) contains the information of only 29 bubbles, even though the complete video recorded 99 bubbles. Fig. 8(b) was intended to illustrate the ongoing analysis, even though the yielded results correspond to the full video length.

Note that Fig. 8(b) reports the shape of bubbles in the video. Conversely, note that the video of bubbles' contours can be recovered from this figure. Several interesting comments can be done on Fig. 8(b). Recall that $y = 0$ is located at the level of the nucleation site, therefore, the blue gaps at $y = 0$ correspond to successive waiting times between bubbles. In addition, note that each horizontal line contains the relevant information of one single frame of the video, for it corresponds to a given time, see for instance Fig. 8(a). Any horizontal line in Fig. 8(b) encompasses at least two bubbles, the first one attached to the heated wall and the second one after its detachment. This feature is inherited from the vertical (y) extent of the region of interest, which was large enough to capture the whole bubble life-cycle. An additional comment is related to the random uncertainty. Note that fringes in Fig. 8(b) are neither regular nor perfectly periodic, which illustrates the need for addressing the random uncertainty. As a final remark, note that the whole time-span in Fig. 8(b) is less than half a second. Thus, each fringe takes almost 17 ms.

Random uncertainty is always related to the experimental setup, and the experiment features. This research was conducted in a quite stable boiling facility. The heat source is applied in an insulated copper rod of 60 mm. diameter and 150 mm. long. In addition, the boiling chamber is also insulated, and takes almost 5 liters of liquid at consigned temperature and pressure. The thermal inertia of the boiling facility is also illustrated by the data acquisition system throughout the experiments. The test section probes changed at most 0.05 K and both precision RTDs, about 0.005 K throughout 4 consecutive seconds, and this pattern is a signature of the boiling facility, for its huge size. Recall that the time scale of each bubble is, at least, three orders of magnitude below the potential response of the operating conditions within the boiling chamber, or the heated surface. Thus, the boiling facility and/or its operation cannot be the source for the observed random uncertainty, even under a wrong manipulation. The video acquisition system was mounted alone and away from mechanical devices, to avoid vibrations. In addition, the camera was switched on and off remotely. As a result, the yielded random uncertainty on bubble growth cannot be related to the operation of the camera. Thus, it can be stated that the random uncertainty is only related to the physical features of this particular experiment.

As a result, a characteristic width function, $\tilde{W}(y,t)$ must be determined. This new characteristic function aims to be the statistically most

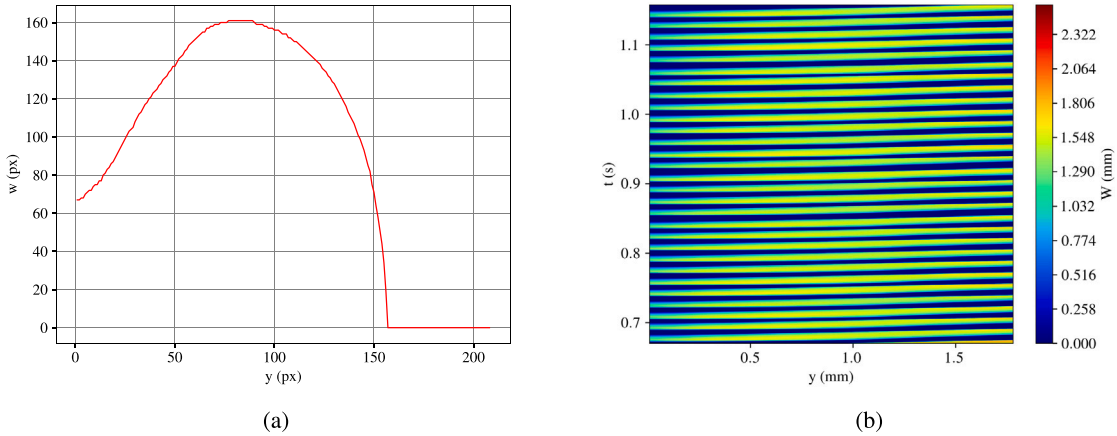

Fig. 8. (a) Captured width for $t = 8.75$ ms. (b) Map of the real video, representing the measured width with time for each y-position.

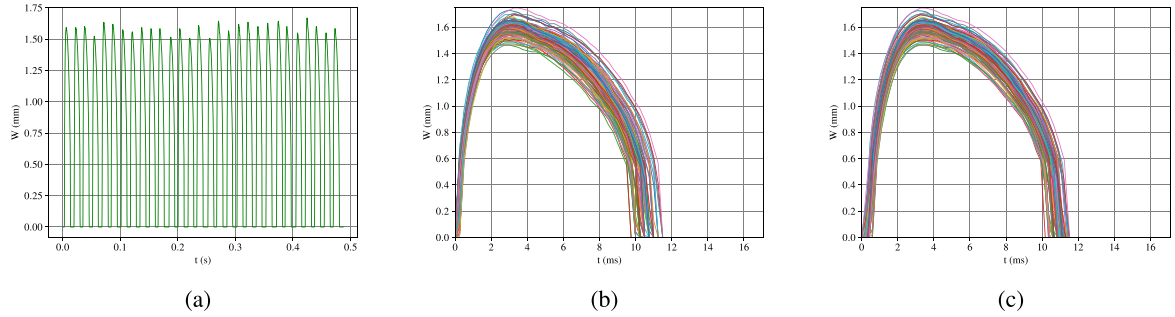

Fig. 9. (a) Captured widths for $y = 0.428 \pm 0.003$ mm. (b) Superposition of the curves for $y = 0.428 \pm 0.003$ mm, after the separation in periods. (c) Superposition of the curves for $y = 0.428 \pm 0.003$ mm, after the re-position minimizing the sum of the square distance between them.

significant width, even though it never took place. Thus, $\tilde{W}(y,t)$ aims to be a sort of ensemble average of all true instances of the bubble. The proposed procedure for yielding $\tilde{W}$ function will be illustrated from Fig. 9(a), which reports the time evolution of bubbles width, W at a given high (y = 0.428 mm) above the nucleation site. Note that similar figures might be rendered for different values of y. The procedure will be based on desegregating each different bubble width period, from each $W = 0$ value to the next one, aggregating the corresponding time with null W value at the end of the period. This transformation is reported in Fig. 9(b). Each different colored line in Fig. 9(b) stands for different bubbles of Fig. 9(a). Legends in this figure were avoided for the sake of clarity. Note that the starting time of all bubbles shown in Fig. 9(b) correspond to moment when each bubble width starts to appear at the observed y. Therefore, all curves in Fig. 9(a) coalesce at the origin, which is nothing else but an artificial feature. Fig. 9(b) also illustrates the presence of random uncertainty, since the width of different bubbles are remarkably different from each other.

Addressing the characteristic width requires a methodology for re-locating each profile in Fig. 9(b). The procedure will also introduce the time random uncertainty, which is not acceptable to be zero at the starting time. Thus, the width profiles in Fig. 9(b) must be relocated (or displaced) in time, in order to minimize the differences between curves. The largest curve in period was taken as reference for the task, and is designated as $W_{ref}(t)$. The time-span for the reference curve runs from $t = 0$ to $t = t_{max}$. Each subsequent curve in Fig. 9(b) is designated as $W_b\left(t - \tau_b\right)$, where the subscript b is an integer ($b \in \mathbb{N}$) that stands for each particular bubble, and τ_b stands for the particular time displacement of each bubble. Note that time displacement of each curve can be expressed as $\tau_b = n_b \epsilon_t$, where ϵ_t is an arbitrarily small time value, an n_b is an integer ($n_b \in \mathbb{N}$) that will be used to minimize the difference between each curve and the reference one. The procedure was carried out with $\epsilon_t = 2.5 \cdot 10^{-5}$ s.

Thus, the difference between both curves was characterized as:

$$D_b^2\left(n_b\right) = \frac{1}{t_{max}} \int_0^{t_{max}} \left[W_{ref}(t) - W_b\left(t - n_b \epsilon_t\right)\right]^2 dt. \tag{3}$$

The function provided by Eq. (3) reaches a minimum under certain value of n_b, which is designated as $n_{b,min}$. Thus, yielding the corresponding time displacement, $\tau_{b,min} = n_{b,min}\epsilon_t$, is straightforward. This time displacement is determined for each curve shown in Fig. 9(b). Fig. 9(c) reports all curves $W_b\left(t - \tau_{b,min}\right)$.

Analyzing the re-positioned curves it is possible to identify two different stages: the first one, where the bubble is passing through the observed y value (the region where W changes with time), and the other one, which is related to the waiting time between consecutive bubbles ($W = 0$ mm). Note that all curves of first stage follow a similar profile, presenting small changes mainly related to their periods, but still preserving some characteristic trend. Thus, the average profile ($\tilde{W}$) of curves in Fig. 9(c) must be addressed and, at the same time, its corresponding random uncertainty.

Despite curves in Fig. 9(c) yield a common pattern, the same physical events for all bubbles are to be identified and correlated. For instance, the initial, maximum and final points in all curves identify the same phenomenological events for successive bubbles. Therefore, all curves in Fig. 9(c) were reproduced with a given and equal number of points, which were equally spaced throughout each curve period. Let P be the total number of points for each curve, and any intermediate point be designated by p index, so that $p \in [1, P]$ and $p \in \mathbb{N}$. Expectedly, similar events occurs for equal pth points throughout different curves. Thus, the mean profile $\tilde{W}(y,t)$ is the average of W_p and t_p mean values for all pth points. Note that the proposed procedure also renders the standard deviation of both time and width for each pth point. Standard deviations from the average are assumed to be the random uncertainty.

An assessment of the proposed procedure is reported in Fig. 10(a), which overlays both the $\tilde{W}$ profile, and all W profiles. Note that both

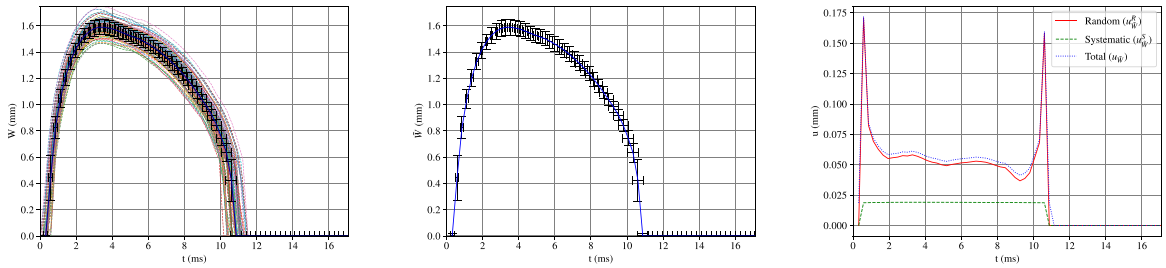

(a) (b) (c)

Fig. 10. (a) Resulting mean curve for $\tilde{W}$ values *versus* time for $y = 0.428 \pm 0.003$ mm with random uncertainties for $\tilde{W}$ and t, over the set of isolated curves (b) Resulting mean curve for $\tilde{W}$ values *versus* time for $y = 0.428 \pm 0.003$ mm with total uncertainties for $\tilde{W}$ (random and systematic). (c) Comparison between random and systematic uncertainties for $y = 0.428 \pm 0.003$ mm.

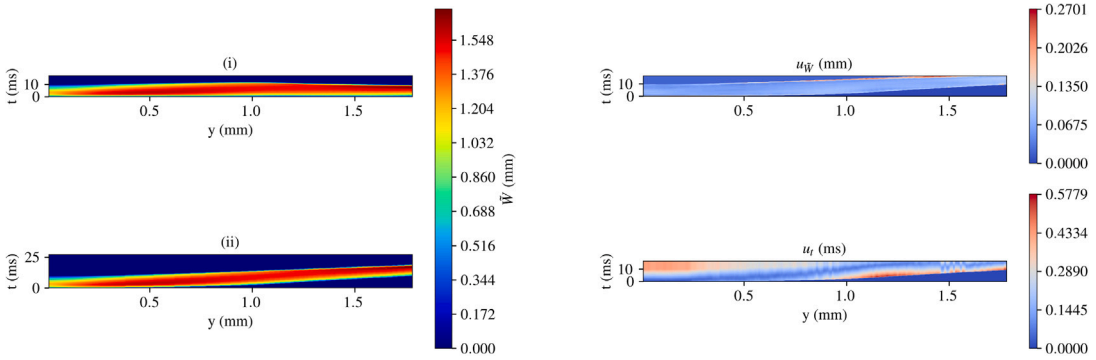

(a) (b)

Fig. 11. (a-i) Mean band with the calculated mean profiles for each y value, without inclination. (a-ii) Final mean band, after the addition of the inclinations. (b) Uncertainties in $\tilde{W}$ and t for the final mean band.

$\tilde{W}$ profile along with its random uncertainty match the whole range of W curves in Fig. 10(a). Besides, for the sake of clarity, Fig. 10(b) reports again the $\tilde{W}$ profile alone, but the error bars show the complete value of uncertainty. The error bars in Fig. 10(b) are the combined result of propagation of systematic and random uncertainty. Recall that systematic uncertainty was inherited from the image calibration and segmentation procedure. It is also interesting compare the random and systematic uncertainties of $\tilde{W}$. Fig. 10(c) depicts both the random and systematic uncertainties of $\tilde{W}$. As general rule, random uncertainty is twice the systematic uncertainty, but at the top and bottom of the bubble the random uncertainty attains one order of magnitude above the systematic uncertainty. Fig. 10(c) also reports the combined uncertainty. Note that whole uncertainty is mainly related to random and, therefore, it seems to be questionable provide uncertainty of bubble features under observation of single, or a few, bubbles. In this point, it is interesting to determine the minimum number of bubbles necessary to yield the proper uncertainty. The full set of details on uncertainty propagation can be found in Appendix A

Regarding the second stage of Fig. 9, where $W = 0$, the average time gap between bubbles is to be determined. This time lapse is meaningful, since it corresponds to the waiting time between consecutive bubbles. The number of all cycles in Fig. 9(a) takes an amount of time. This time, divided by the number of cycles, provides the average period of one single cycle. Thus, the waiting time is yielded by subtracting the first stage time, already available, from the complete cycle period.

Note that Figs. 9 and 10 illustrate the procedure for a given depth, i.e. $y = 0.428 \pm 0.003$ mm. As a result, previous paragraphs describe the procedure implemented to yield the average function $\tilde{W}$ at $y = 0.428$ mm. The same procedure was carried out for the full range of y values within the region of interest. The resulting data is reported in Fig. 11(a)(i). Note that $\tilde{W}$ in Fig. 11(a)(i) starts to grow at the initial time for the full range of y. This artificial feature is not physical, and is inherited from the already described procedure. Recall the proposed procedure moved all profiles to begin at null time and, therefore, the delay associated to each depth, y, is lost. Otherwise put, the slope of fringes in Fig. 8(b) is $\left(\frac{\partial y}{\partial t}\right)_W$, which is the ascending velocity of the bubble at each level, was disregarded by the proposed procedure.

Therefore, a reference value must be taken for the ascending velocity of the fringes. The proposal will be based on the ascending velocity of each bubble apex, which can be determined as $\left(\frac{\partial y}{\partial t}\right)_b^{apex}$. Fig. 8(b) contains, again, the proper information: the inverse of the slope of the upper edge of each colored fringe is the velocity we are looking for. Thus, the apex velocities for all bubbles at any given vertical distance from the nucleation site, $v_b^{apex}(y) = \left(\frac{\partial y}{\partial t}\right)_b^{apex}$ was calculated and, again, the average velocity was determined in the conventional manner:

$$\tilde{v}^{apex}(y) = \frac{1}{B}\sum_{0}^{B} v_b^{apex}(y); \tag{4}$$

where B stands for the total number of bubbles captured in the video.

Given $\tilde{v}^{apex}(y)$, each δy increment in Fig. 11(a)(i) must displace a time interval (with null width) equal to $\delta t(y) = \frac{\delta y}{\tilde{v}^{apex}(y)}$. The result of this procedure is reported in Fig. 11(a)(ii), where a null width band of thickness $\delta t(y)$ was added at the bottom of the figure. Note that Fig. 11(a)(ii) resembles Fig. 9(c), albeit the former corresponds to a synthetic bubble that never took place and, for sure, will never take place, even though being the most representative bubble. It renders the function $\tilde{W}(y,t)$ for the most representative bubble.

The proposed procedure also yields the global uncertainty of both the average width, $u_{\tilde{W}}$, and time, u_t. Fig. 11(b) shows $u_{\tilde{W}}$ (upper map) and u_t (lower map). Note that, as previously stated, the maximum values of $u_{\tilde{W}}$ took place at both the top and bottom of the bubble. This

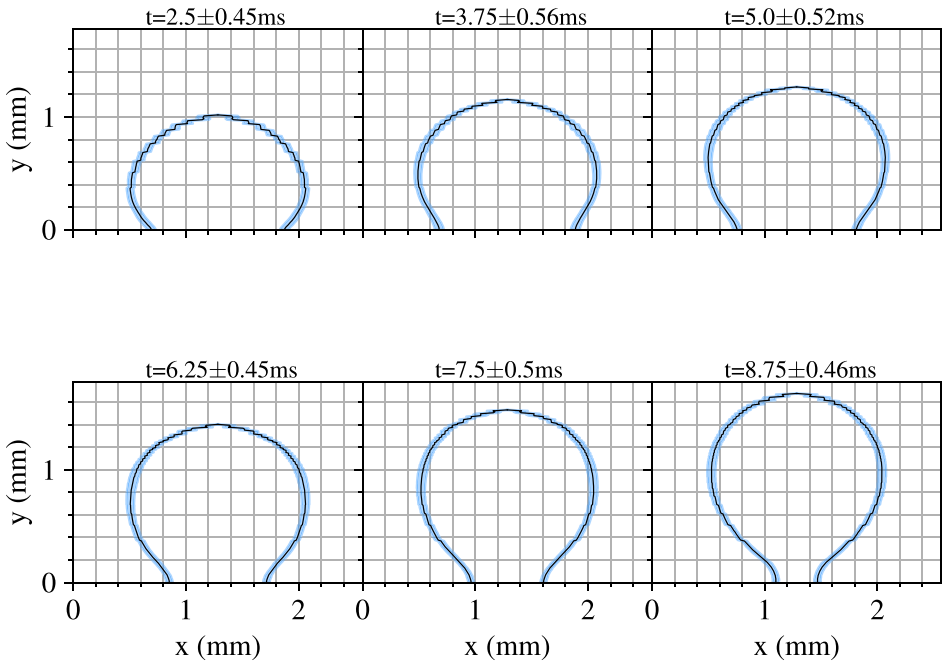

Fig. 12. Example of the profile for the typical bubble and its uncertainty (blue region around the lines).

Table 1
Table with some points of the typical bubble life-cycle, showing the width $\tilde{W}$ with its uncertainties $u_{\tilde{W}}$ and u_t for some (t, y) values. The dimensions of $\tilde{W}$ and $u_{\tilde{W}}$ are in mm, while u_t is in ms. The legend to interpret the table can be seen below the data.

y(mm) / t(ms)	0.009		0.18		0.351		0.522		0.693		0.865		1.036		1.207		1.378		1.549		1.549	
0.0	0.0	0.019	0.0	0.0	0.0	0.0	0.0	0.0	0.0	0.0	0.0	0.0	0.0	0.0	0.0	0.0	0.0	0.0	0.0	0.0	0.0	0.0
		0.042		0.0		0.0		0.0		0.0		0.0		0.0		0.0		0.0		0.0		0.0
1.5	1.065	0.059	1.32	0.062	1.382	0.063	1.123	0.071	0.904	0.074	0.0	0.019	0.0	0.0	0.0	0.0	0.0	0.0	0.0	0.0	0.0	0.0
		0.05		0.046		0.073		0.1		0.142		0.251		0.0		0.0		0.0		0.0		0.0
3.0	1.206	0.071	1.43	0.067	1.569	0.061	1.546	0.063	1.437	0.074	1.128	0.084	0.484	0.092	0.0	0.0	0.0	0.0	0.0	0.0	0.0	0.0
		0.115		0.108		0.08		0.075		0.098		0.194		0.397		0.0		0.0		0.0		0.0
4.5	1.128	0.074	1.313	0.066	1.491	0.055	1.579	0.061	1.559	0.073	1.418	0.084	1.12	0.073	0.203	0.092	0.0	0.0	0.0	0.0	0.0	0.0
		0.185		0.174		0.121		0.086		0.075		0.141		0.326		0.531		0.0		0.0		0.0
6.0	0.903	0.059	1.099	0.063	1.36	0.057	1.515	0.056	1.555	0.066	1.519	0.077	1.384	0.079	1.037	0.06	0.204	0.095	0.0	0.0	0.0	0.0
		0.255		0.24		0.174		0.122		0.091		0.098		0.256		0.447		0.417		0.0		0.0
7.5	0.642	0.053	0.827	0.051	1.139	0.052	1.391	0.056	1.495	0.062	1.531	0.072	1.48	0.077	1.324	0.07	1.042	0.072	0.0	0.019	0.0	0.019
		0.326		0.307		0.23		0.169		0.133		0.084		0.188		0.363		0.346		0.468		0.468
9.0	0.307	0.062	0.423	0.058	0.819	0.052	1.178	0.051	1.362	0.057	1.487	0.067	1.512	0.072	1.447	0.071	1.293	0.072	0.955	0.074	0.955	0.074
		0.397		0.374		0.287		0.219		0.184		0.11		0.125		0.28		0.277		0.377		0.377
10.5	0.0	0.019	0.0	0.019	0.0	0.019	0.832	0.049	1.153	0.049	1.379	0.059	1.488	0.069	1.507	0.071	1.438	0.069	1.239	0.07	1.239	0.07
		0.429		0.414		0.337		0.27		0.238		0.157		0.082		0.199		0.211		0.288		0.288
12.0	0.0	0.019	0.0	0.019	0.0	0.019	0.0	0.019	0.053	0.041	1.21	0.051	1.406	0.059	1.508	0.067	1.518	0.071	1.429	0.076	1.429	0.076
		0.429		0.414		0.337		0.299		0.293		0.212		0.091		0.125		0.153		0.204		0.204
13.5	0.0	0.019	0.0	0.019	0.0	0.019	0.0	0.019	0.0	0.019	0.0	0.019	1.129	0.162	1.478	0.049	1.537	0.064	1.532	0.084	1.532	0.084
		0.429		0.414		0.337		0.299		0.294		0.255		0.144		0.08		0.115		0.134		0.134
15.0	0.0	0.019	0.0	0.019	0.0	0.019	0.0	0.019	0.0	0.019	0.0	0.019	0.0	0.019	0.686	0.2	1.489	0.147	1.608	0.065	1.608	0.065
		0.429		0.414		0.337		0.299		0.294		0.255		0.175		0.109		0.119		0.109		0.109

y(mm) / t(ms)	y[mm]	
t[ms]	$\tilde{W}$[mm]	$u_{\tilde{W}}$[mm] / u_t[ms]

effect will be clearly illustrated in the coming bubble reconstruction. Besides, the time uncertainties map reported in Fig. 11(b) (lower map) shows that certain relevant events, such as the apex location on time is not straightforward. This feature is related to the fact that not all 99 studied bubbles takes the same time for the bubble life-cycle, and this is propagated to all stages of bubble growth.

Previous scheme allows for the reconstruction of the average bubble along with its uncertainty. Functions $\tilde{W}(y,t)$, $u_{\tilde{W}}$, and u_t can be used to report some instances of the bubble profile, i.e. the six shown in Fig. 12. Recall that function $\tilde{W}(y,t)$ provides the average bubble shape for all frames of the high speed (4000 fps) video and, therefore, the time resolution can hardly be reported in a figure. Note that Fig. 12 also provides the uncertainty values on both shape and time, according to the described procedure. Recall these kind of information is of utmost importance for scientists concerned on bubbles growth models, but also and mainly, for eventual assessment of numerical procedures. As a result, the proper manner to report the complete set of data is through an extensive table.

Data reported in Table 1 was yielded from the full set (99) of bubbles in the video. The full set of data is reported in the supplementary material of this paper (Appendix C). Therefore, it is interesting to address the minimum number of bubbles necessary to attain significant results, both on average and uncertainty of bubble shape. The convergence of uncertainty values will be taken as the reference for the assessment of the minimum required number of bubbles. Fig. 13 provides an insight on how both random and systematic uncertainty behaves when different number of bubbles is considered.

Figs. 13(a), 13(b), and 13(c) report the random uncertainty at three different vertical distances from the nucleation site, for 25, 50, 75 and 99 bubbles. In the same fashion, Figs. 13(d), 13(e), and 13(f) reports the systematic uncertainty. Note that systematic uncertainty of an average value decreases as long as more instances are considered, according to Eq. (A.2). As a result, Figs. 13(d), 13(e) suggest that almost 75 bubbles are necessary to address systematic uncertainty, and this statement seems to be valid for the whole range of y values.

However, as already mentioned, note that systematic uncertainty is not the relevant one, since the scale of figures reporting the random uncertainty is one order of magnitude above the systematic one. Once again, peaks in Figs. 13(a), 13(b), and 13(c) correspond to apex and bottom of the bubble. Since the extremes of the bubbles are singularities, both in the random value and its derivative, it seems pertinent to focus the attention on intermediate values. Fig. 13(b) shows that more than 25 bubbles are necessary to properly address the random

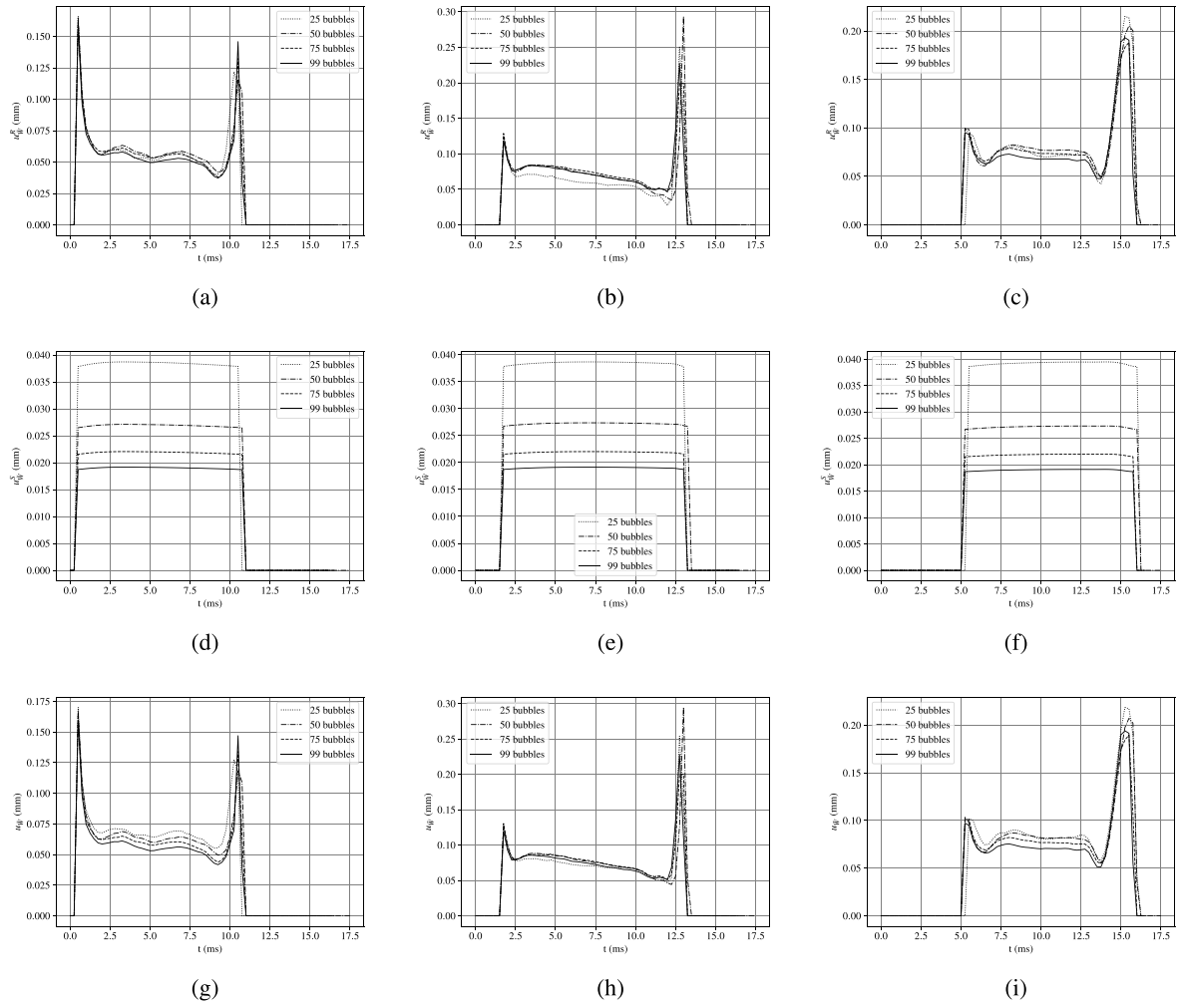

Fig. 13. Impact of the considered bubbles' number on random (a,b,c), systematic (d,e,f) and total (g,h,i) errors, considering $y = 0.428 \pm 0.003$ mm (a,d,g), $y = 0.856 \pm 0.006$ mm (b,e,h) and $y = 1.284 \pm 0.009$ mm (c,f,i).

uncertainty. Previous statement could also be posed from observation of Fig. 13(c). As a result, it can be concluded that a minimum of 25 bubbles are necessary to provide the quality of data similar to the reported herein. Nevertheless, a smaller amount of bubbles could also be used to yield the average bubble contours, and these data would not be mistaken. Working with a smaller amount of bubbles would bring forth a non negligible impact on the random uncertainty of contours. Recall that random uncertainty cannot be disregarded when reporting the bubble contour and, regretfully, this is not commonly considered in the open literature.

In this section the new methodology for bubble's characteristics determination through the calculation of the typical bubble was developed. Thus, the procedure, after getting the values of $W(y,t)$ from image-processing analysis, can be summarized in the following steps:

1. Find the beginning and the end of each bubble for each y-value(period where it is a bubble passing through the observer y plus the waiting time before the next bubble is identified) and isolate the curves (Fig. 9(b));
2. Re-allocate the curves minimizing the square of the distance between them (Eq. (3)), considering only the period where there is a bubble passing through the observed y, still for each y-value (Fig. 9(c));
3. Divide the re-allocated curves into the same number of points, P, and calculate the mean position, $\tilde{W}$ and t, for each point. Note that at this step the standard deviations in t and W, namely $u_{\tilde{W}}$ and u_t, are also obtained (Fig. 10). This must be performed for each y value, as the previous steps;
4. Calculate the average waiting time from all the waiting times at the observed y and add it to the mean curve $\tilde{W}$. At this step, the mean band with the mean profiles for each y is already determined, but without the slope related to the speed of the bubbles (Fig. 11(a)-i);
5. Determine for each y the slope of the mean band by the calculation of the t-average bubble apex velocity, $\tilde{v}^{apex}(y)$, using Eq. (4);
6. Correct the mean band in t by adding a time interval, $\delta t(y) = \frac{\delta y}{\tilde{v}^{apex}(y)}$, before the beginning of the mean band in each t. This last step yields the complete mean band and, consequently, the typical bubble life-cycle (Fig. 11(a)-ii).

The methodology can be used in a generalized manner. We have already developed some preliminary tests on two coalescing growing bubbles, and the algorithm seems to work properly, but more work must be developed prior to expose our findings to the scientific community. In what follows, data on bubble volume, frequency, apparent contact angle, and dry contact will be post-processed.

3.2. Data analysis

Considering axial symmetry of the average bubble, its volume was calculated as:

$$\forall(t) = \int_0^{y_{apex}} \pi \frac{\tilde{W}^2(y,t)}{4} dy = \frac{\pi}{4} SF \sum_{n=1}^{N_{y,apex}} \tilde{W}^2(nSF,t), \quad (5)$$

where y_{apex} is the maximum y value of the bubble, and $SF = 8.53$ mm/px, stands for the scaling factor. Note that $N_{y,apex}$ in Eq. (5) corresponds to the total number of pixels between the nucleation site and the bubble apex, and can also be determined as $N_{y,apex} = \frac{y_{apex}}{SF}$. Red curve in Fig. 14(a) yields the function $\forall(t)$ given by Eq. (5).

Assessment of both previous volume values and the corresponding uncertainty will next be addressed. Two procedures will be used to determine both the volume and uncertainty that, in addition, will also validate the whole methodology proposed herein. Perhaps, the most intuitive procedure to determine the volume uncertainty is based in the calculation of the maximum and minimum possible volumes of blue regions reported in Fig. 12. The upper and lower limits for the bubble volume are given by $\tilde{W} + u_{\tilde{W}}$ and $\tilde{W} - u_{\tilde{W}}$, respectively. Thus,

$$u_{\forall} = \frac{\forall_{ul} - \forall_{ll}}{2} = \frac{1}{2}\left[\frac{\pi}{4} SF \sum_{n=1}^{N_{y,apex}} (\tilde{W} + u_{\tilde{W}})^2 (nSF,t) - \frac{\pi}{4} SF \sum_{n=1}^{N_{y,apex}} (\tilde{W} - u_{\tilde{W}})^2 (nSF,t)\right]. \quad (6)$$

Results of volume uncertainty yielded by Eq. (6), and time uncertainty, u_t, are reported with black crosses in Fig. 14(a). The volume of the characteristic bubble, $\forall(t)$, was additionally computed from the bare data of the full set (99) of bubbles. Recall that taken video can be summarized in a similar fashion than reported in Fig. 8(b). As a result, the time evolution of volume for each y value in Fig. 8(b) can be also calculated by Eq. (5), but considering now $W(y,t)$ instead of $\tilde{W}(y,t)$. The same procedure for time displacement of width curves, recall $\tau_{b,min}$ and P characteristic events/points already illustrated in Figs. 9 and 10, was applied to volume curves. Yielded results are represented by the dashed line in Fig. 14(a), and the corresponding uncertainty is reported by the blue colored region. As expected, both volume curves almost match each other, with only small deviations within both uncertainty regions. Thus, the proposed procedure to provide the bubble contour, and its corresponding uncertainty, keeps physical coherence. Note that bubble volume slightly decreases before detachment. This peculiar feature could be related in a great extent to the complex hydrodynamic behavior of the bubble detachment process characterized by small compressibility effects and volume changes noted in the videos. At this point, yielding the equivalent radius is straightforward. Assuming the bubble as a perfect sphere, $R_{eq} = (3\forall/4\pi)^{1/3}$. The function $R_{eq}(t)$ is shown in Fig. 14(b).

The assessment of both accuracy and precision of the new methodology is of utmost importance. Recall that bubble volume is commonly used to confront experimental results to analytical models, and vice versa. Thus, given that the procedure to calculate both the volume and its uncertainty was already introduced, it seems pertinent applying the proposed methodology to pictures/videos reported elsewhere, and compare the yielded results. A benchmark exercise was carried out considering the closed set of pictures reported in [16]. A comparison of the yielded results following the approach reported herein and the one applied in [16] can be found in Appendix B. The excellent agreement between both set of results strengthen the validation of the procedure introduced herein. It is interesting to note, in addition, that results from [16] were only yielded for one single bubble. Thus, the uncertainty bars are defined from our estimation of the systematic uncertainty considering that [16] did not report it. We assumed that the bubble uncertainty was $u_{w_b} = 4$ px, which seems reasonable according to yielded results (see Fig. B.1).

Another usually studied feature of the bubble is the dynamic contact angle, $\phi(t)$, that can also be obtained from Table 1 and/or the corresponding supplementary data. The simple secant method was used for the angle calculation [32]. This methodology is based on two points identification: the first one located at the tipple line (where the three phases meet), whereas the second one is located within the bubble interphase, in the near vicinity of the triple line. The coordinates of the first point will be designated as $(x_{tl}, y_{wall}) = (x_{tl}, 0)$. The second point was located arbitrarily near the triple line, i.e. 5 pixels above the nucleation site. Thus, the vertical coordinate of this second point was $y_{nvtl} = 0.0428 \pm 0.0003$ mm according to the scale factor SF, and represents approximately 2.5% of the bubble maximum height. The corresponding x_{nvtl} is given by the bubble interphase geometry at the given y_{nvtl} value. As a result, the contact angle can be calculated through Eq. (7).

$$\phi(t) = \arctan\left(\frac{y_{nvtl}(t)}{x_{nvtl}(t) - x_{tl}(t)}\right) \quad (7)$$

Fig. 15(a) shows the function $\phi(t)$ for the 99 studied bubbles. Expectedly, this figure illustrates that both the averaged contact angle and its uncertainty determination is not straightforward and, therefore, observation of details on each bubble seems to be pertinent. Fig. 15(b) shows a detailed visualization of the dotted square region in Fig. 15(a). Note that Fig. 15(b) shows a quite repetitive pattern for the contact angle on successive bubbles. Thus, this pattern deserves to be postprocessed and analyzed.

Again, the averaging procedure reported herein for $\tilde{W}$ determination was applied for yielding the contact angle. In the same manner, the procedure to determine the uncertainty of the contact angle can be found in Appendix A, and follows the same methodology than the exposed for the averaging procedure. Besides, the time uncertainty of the contact angle was estimated as the maximum time uncertainty yielded by Table 1 for the pair of points required for the calculation, i.e. $\max\{u_t(y_{nvtl},t); u_t(0,t)\}$.

Fig. 16(a) shows the averaged dynamic contact angle of the bubble. Recall that dynamic contact angle is usually related to the velocity of the triple line. Therefore, reporting the movement of the triple line seems to be pertinent. The triple line advance or receding can be characterized through the dry radius R_d, which represents the circular portion of the wall in contact with the gas phase. R_d can easily be found from the typical bubble shape, taking a half of the $\tilde{W}$ value at $y = 0$ mm. The values of $R_d(t)$ are found in Fig. 16(b).

Simultaneous observation of Figs. 14 and 16 provides additional information. Fig. 14(a) shows that bubble growth encompasses a first growth stage, where the volume changes with time and takes almost 4 ms. The second stage might be associated to the region where the bubble volume is almost constant. This second stage is clearly observable in Fig. 14(a) and takes more than 4 ms, until bubble detachment. These two stages can be also identified in Figs. 16(a) and 16(b). Note that Fig. 16(b) provides the dry radius, R_d and, therefore, its derivative reports the triple line velocity. Note that R_d grows throughout the first stage, which suggests that an advance dynamic contact angle takes place. Conversely, Fig. 16(b) shows that second stage is associated to a retraction of the triple line and, therefore, to a somehow receding contact angle, see Fig. 16(a).

Besides, the proposed procedure provides an additional insight regarding the bubble dynamics. The intervening forces throughout the bubble growth were desegregated according to the model of Zeng, Klausner and Mei [33]. The ongoing force analysis will follow the model of [33]. Note that buoyancy and surface tension forces are usually reported in the basis of bubble shape observation. Regretfully, determining the other set of intervening forces was not straightforward. Nevertheless, it becomes possible with the new methodology. The model from [33] relates the bubble acceleration to the applied set of

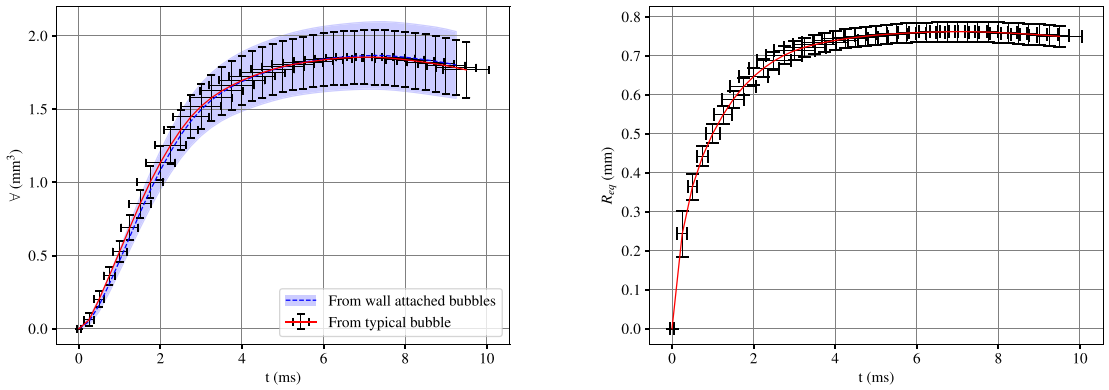

Fig. 14. (a) Typical bubble's volume evolution with time, while still attached to the wall. The red curve shows the results from the shape of the averaged bubble reported in Fig. 12 and/or Table 1. The dashed black line was calculated from the volume of each particular bubble at each frame from the original video, and the average was processed with the best fitting technique driven by time ($\tau_{b,min}$) displacement. (b) Typical bubble's equivalent radius with time, while still attached to the wall.

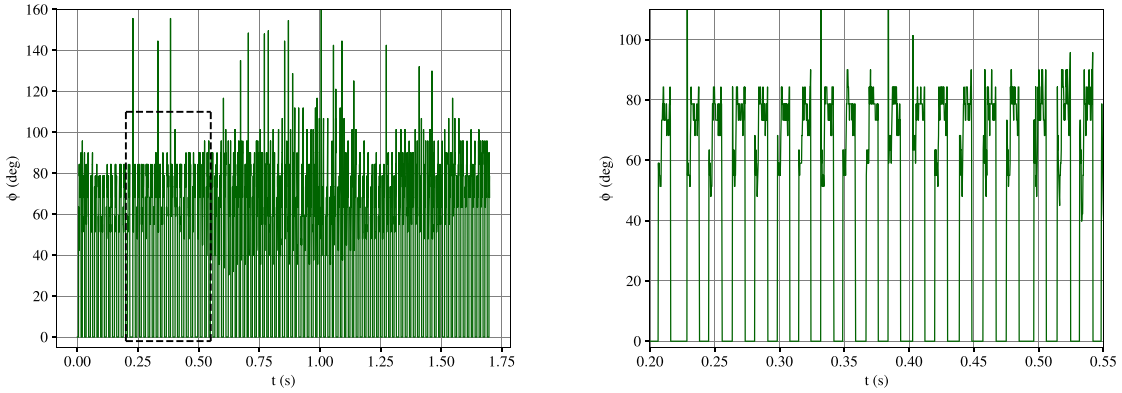

Fig. 15. (a) Local bubble's contact angle from experimental data (b) detailed visualization of the region between dashed lines in previous plot.

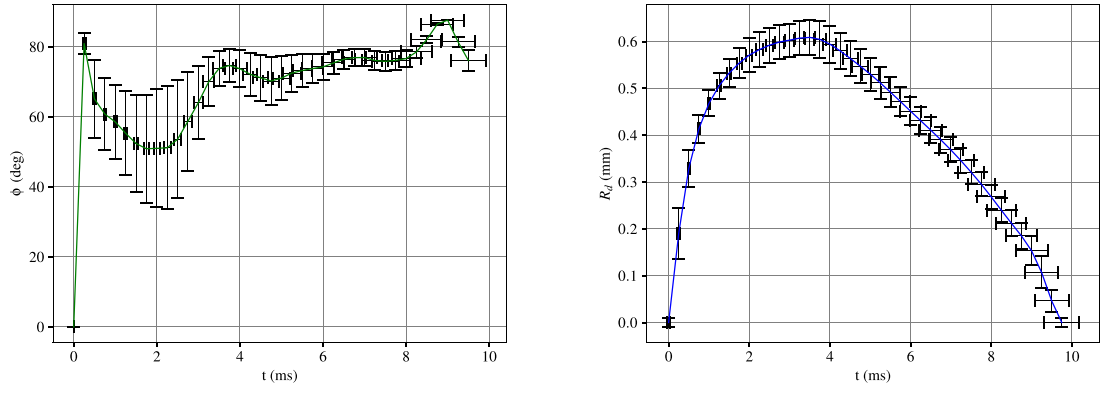

Fig. 16. Averaged dynamic contact angle (a) and typical bubble's dry radius (b).

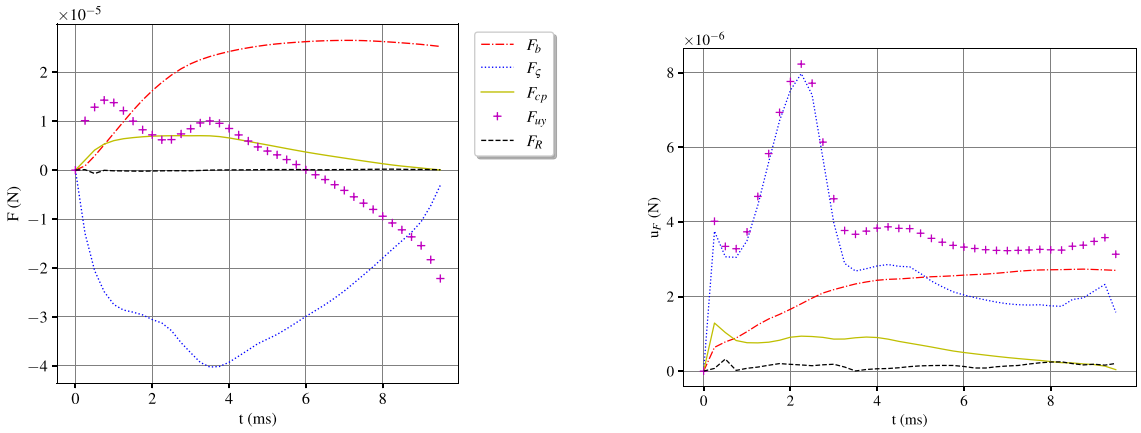

Fig. 17. Forces acting on the bubble during its growth period (a) and its uncertainty from propagation (b).

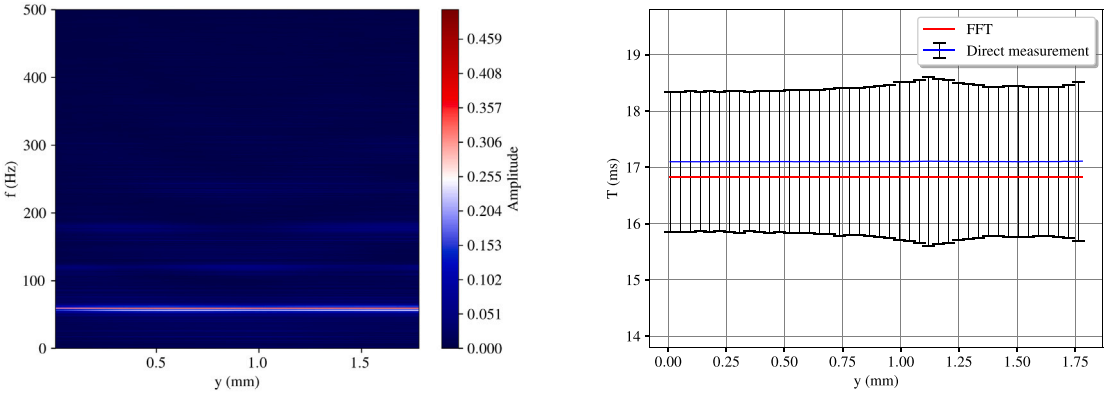

Fig. 18. FFT output (a) and comparison between the mean period calculated from FFT and from direct measurement of raw data (b).

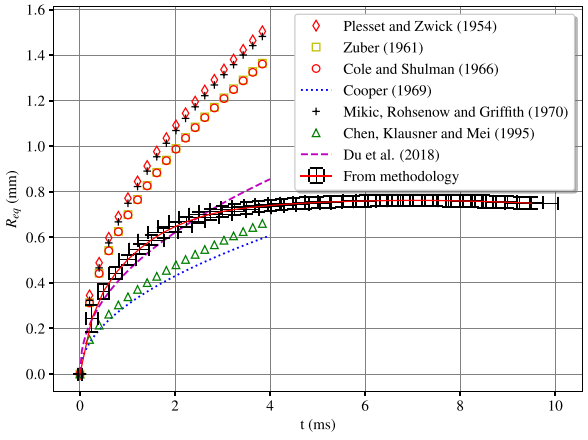

Fig. 19. Comparison between the equivalent radius captured by our procedure from the experimental data and literature relations.

forces as:

$$\rho_v \forall \frac{dv}{dt} = F_b + F_\varsigma + F_{cp} + F_L + F_{uy}; \tag{8}$$

where F_ς stands for the vertical component of the surface tension force, F_{cp} is the vertical component of the contact pressure force, F_b is the buoyancy force, F_L is the lift force due to the induced velocity field from preceding bubble, and F_{uy} stands for the "unsteady growth force", in words of [33]. This force accounts for the effect of mass addition and other dynamic effects that were not accounted by the other forces such as the drag force.

Moreover, the only term in the LHS of Eq. (8) is the bubble inertia, which is characterized by the acceleration of the vapor bubble mass. Note that the proposed procedure yields the bubble velocity, v, at each level, y, above the nucleation site, i.e. recall the fringes slope in Fig. 11(a). Therefore, the time evolution of the LHS term in Eq. (8) can now be addressed. In what follows we will designate the LHS of Eq. (8) as F_R.

The expressions provided by [33] for the terms in the RHS of Eq. (8) are:

$$F_b = \forall(\rho_l - \rho_v)|\mathbf{g}|. \tag{9}$$

$$F_{\varsigma} = -2\pi R_d \varsigma \sin(\phi); \tag{10}$$

$$F_{cp} = \pi R_d^2 \frac{2\varsigma}{R_r}; \tag{11}$$

where ς stands for the surface tension, ρ_l and ρ_v stand for the liquid and vapor densities, respectively, g is the gravitational acceleration, and R_r is the radius of curvature at the base of the bubble. Zeng, Klausner and Mei proposed that $R_r \approx 5R$, which was also adopted by Zhou et al. [34] in their research.

Zeng, Klausner and Mei [33] also provide an approach to estimate F_L, even though they also suggest this force to be negligible. They calculate the force on the growing bubble as the pressure integral over its surface provided by the solution of potential flow. They propose:

$$F_L = \frac{75}{16}\rho_l v^2 R^2 \left(\frac{R}{H}\right)^8; \tag{12}$$

where H is the vertical distance between the center of the preceding bubble and the one attached to the wall.

Given that authors of [33] suggested that lift force might be small, it seems pertinent addressing a gross estimation of this magnitude. The maximum possible value of F_L can be estimated by maximizing all factors in Eq. (12). Therefore, we will consider (i) the maximum bubble velocity (ii) the maximum value of bubble radius, and (iii) the minimum value of H. For the instance studied herein, the maximum value of v is 0.140 m/s, the maximum value of R is 0.76 mm, and the minimum value of H is 2.70 mm. Under previous considerations the maximum force F_L becomes $3.0 \cdot 10^{-9}$ N.

Finally, the vertical component of the "unsteady growth force", F_{uy}, must be determined. Note the proposed approach allows for yielding F_{uy} through Eq. (8), since all other terms were analytically determined and $F_L \approx 0$. However, recall that calculating F_{uy} is not straightforward. Indeed, [33] reported four different semi-empirical approaches to address it, illustrating the necessity of further experimental evidence. Thus, our new approach could also be used to calibrate the semi-empirical models for F_{uy}. Here this work will only report F_{uy} for the studied instance, for it is mainly intended to illustrate the possibilities of this new methodology.

Fig. 17(a) shows both the vertical forces acting on the bubble and its acceleration (F_R = LHS of Eq. (8)), while Fig. 17(b) reports its respective uncertainties. Note the proposed approach provides absolute uncertainties one order of magnitude below the measured magnitude. Therefore, Fig. 17(b) also illustrates the feasibility of the proposed methodology to yield dynamical results on bubble growth.

In view of Fig. 17, it is clear that the resultant force approaches to zero after $t \approx 4$ ms. This instant matches to the time when the bubble's volume stops to change considerably. It allows us to conclude that the bubble is momentarily in equilibrium, and the forces are balancing each other, as represented by Eq. (13). It is interesting to note that, besides the acceleration of the bubble is almost zero in this stage, its shape does not stop to change (see for example the dry radius in Fig. 16(b)). As we can identify in Fig. 17, the forces' changes compensate each other. When this equilibrium falls apart, the bubble is detached from the wall and a new cycle begins.

$$0 = F_b + F_{\varsigma} + F_{cp} + F_{uy} \tag{13}$$

It could be argued that FFT from $W(y,t)$ instead of $\tilde{W}(y,t)$ cannot yield quite precise and accurate results on the average bubble. However, Fig. 18(b) illustrates exactly the opposite. The period calculated from the strongest frequency of the FFT ($\frac{1}{f}$) for the full range of y within the region of interest is the red curve. Note that the FFT yields an almost constant frequency that does not depend on y. Besides, the blue line shows the mean periods with the corresponding standard deviations previously calculated for the two stages shown in Fig. 10(b), also for the full range of y. The agreement between both periods is remarkable, with a maximum absolute difference about $1.30 \cdot 10^{-4}$ s. Given that mean period is 0.017 s, the difference between both methods is about 0.8% of the mean period. As a result, the FFT of the function $W(y,t)$ constitutes a valid shortcut for yielding the average bubble's nucleation frequency. Note that FFT output in Fig. 18(b) is not concerned with the uncertainty. However, the inverse of the spectra shown in Fig. 18(a) yields again Fig. 8(b) with negligible deviation, though not shown for the sake of brevity.

An additional and final assessment of the proposed methodology will next be developed. Confronting the bubble equivalent radius (R_{eq} as a function of time) with available correlations will provide an additional benchmarking and, besides, it will illustrate the convenience of further experimental evidence. Recall that Fig. 14(b) already provided the yielded equivalent radius evolution with time.

A wide variety of correlations for bubble growth can be found in the literature. Some of them are intended to model the bubble growth in a superheated fluid, see for instance the relations developed by Plesset and Zwick [35] and further by Mikic, Rohsenow and Griffith [2]. Besides, the expression developed by Zuber [36] for bubble growth in a non-uniform field was also addressed in the comparison.

Expressions on the growth rate of bubbles attached to heated wall, which are more related to the experimental study provided herein, will also be considered. The expressions developed by Cole and Shulman [37], by Cooper [38], by Chen, Klausner and Mei [39] and a more recent study developed by Du et al. [40] were addressed for this comparison exercise.

Fig. 19 shows overlaid all mentioned correlations with the results yielded by the new methodology. Fig. 19 illustrates that all correlations seems to fit each other, as well as the experimental results reported herein, for the very early stage of the bubble growth. However, all curves depart from each other for later time stages. Indeed, only the correlation proposed by Du et al. matches the experimental growing evolution within the uncertainty, up to almost the maximum volume of the bubble, around the time $t = 3$ ms. This best fit might be related to the fact that correlation of Du et al. took into account the effect of reduced pressure. There is a final stage of the life-cycle where essentially the bubble does not change its volume. In this final stage, that lasts more than half the life-cycle, the bubble changes its shape, even though its volume is almost kept. This last stage could not be reproduced by any of the mentioned correlations. Thus, it seems that experimental evidence, such as the one reported herein, is pertinent.

4. Conclusions

A new methodology to experimentally analyze the bubble growth and life-cycle of bubbles was proposed, developed, validated and applied to HFE-7100 fluid from 3M company under saturated conditions. The methodology takes into account the complete set of information of a video, both in space and time, and yields the most plausible instance of the bubble shape along with the corresponding uncertainty. Several general conclusions can be extracted:

- Variability of consecutive bubbles is relevant and, therefore, a small number of bubbles does not suffice to characterize the bubble growth. As relevant as the bubble shape is its corresponding uncertainty, that is commonly omitted in scientific literature.
- Under the operating conditions imposed herein, a minimum of 25 bubbles were necessary to properly address the bubble features throughout its life-cycle.
- Matching experimental results is of utmost importance for numerical scientists. Detailed information on bubble growth is scarce and in general, according to previous conclusion, of questionable quality. This research is released with a supplementary file that contains complete and detailed information on the bubble shape. This information is relevant to determine both the kinematics and also the dynamic features of the bubble.

- The forces on the bubble as a function of time can be determined from the proposed methodology, as well as its uncertainty. This shows the feasibility of the proposed methodology to yield dynamical results on bubble growth, providing a valuable database for building theoretical and semi-empirical models of this phenomena.
- The bubble frequency seems to be independent on the vertical distance to the nucleation site. This feature, along with the FFT analysis, allows to determine the bubble frequency with almost null uncertainty, in this case below 1.0%.
- The model proposed by Du et al. [40] for the equivalent radius curve was the one best fit our experimental data. However the model of Du et al. fails to predict the final stage of the bubble life-cycle. This featur illustrates the necessity of more experimental evidence.

Note this work was mainly intended to propose a new methodology to analyze bubble features. The post-processed data reported herein were only reported to show the possibilities of the supplementary data released with this research.

CRediT authorship contribution statement

Ivan Talão Martins: Writing – review & editing, Writing – original draft, Visualization, Validation, Supervision, Software, Resources, Project administration, Methodology, Investigation, Funding acquisition, Formal analysis, Data curation, Conceptualization. **Pablo Fariñas Alvariño:** Writing – review & editing, Writing – original draft, Visualization, Validation, Supervision, Software, Resources, Project administration, Methodology, Investigation, Funding acquisition, Formal analysis, Data curation, Conceptualization. **Luben Cabezas-Gómez:** Writing – review & editing, Writing – original draft, Visualization, Validation, Supervision, Software, Resources, Project administration, Methodology, Investigation, Funding acquisition, Formal analysis, Data curation, Conceptualization.

Declaration of competing interest

The authors declare that they have no known competing financial interests or personal relationships that could have appeared to influence the work reported in this paper.

Data availability

This research is released with free supplementary data.

Acknowledgments

The authors acknowledge the support received from FAPESP, Brazil (São Paulo Research Foundation, grants 2016/09509-1, 2019/21022-9, 2021/14338-0 and 2023/02383-6) and CNPq, Brazil (National Council for Scientific and Technological Development, process 305941/2020-8). Surface treatment of the test section and nucleation sites were developed by José Manuel Amado Paz and Alberto Ramil Rego, from the Industrial Applications of Laser Laboratory at the University of A Coruña.

Appendix A. Uncertainty propagation

Let the magnitude z be a function of a set of uncorrelated variables x_i, so that $z = f\left(x_1, \ldots, x_i, \ldots, x_N\right)$. Then, the uncertainty of z can be yielded in the following manner:

$$u_z^2 = \sum_{i=1}^{N} \left(\frac{\partial f}{\partial x_i}\right)^2 u_{x_i}^2. \tag{A.1}$$

Results reported in this work rely on the average width, $\tilde{W}(y,t)$, of a set of different bubbles. Lets identify each bubble in the video with the subscript b, and the total number of bubbles with B, so that $b = 1, 2, \ldots, B$.

Recall that systematic uncertainty is inherited from the scaling and segmentation procedures. Width in mm is given by: $W_b(y,t) = w_b(y,t) \cdot SF$, where w_b stands for the width in pixels, and SF for the scaling factor. Both the scaling factor, SF, and width, w_b, are affected by their corresponding systematic uncertainties u_{w_b} and u_{SF}, respectively. Both uncertainties are uncorrelated, thus, following Eq. (A.1) the resulting systematic uncertainty for the scaled width is: $u_{W_b} = \sqrt{\left(SF \cdot u_{w_b}\right)^2 + \left(w_b \cdot u_{SF}\right)^2}$.

Besides, as exposed in Section 3.1, the W_b profiles pass through an averaging procedure to obtain the $\tilde{W}(y,t)$ values. According to Eq. (A.1), the systematic uncertainty after the averaging procedure is:

$$u_{\tilde{W}}^S = \frac{1}{B}\sqrt{\sum_{b=1}^{B} u_{W_b}^2}. \tag{A.2}$$

In addition, random uncertainty of the average $\tilde{W}$ profile is defined as the standard deviation of all W profiles from the average $\tilde{W}$. Thus,

$$u_{\tilde{W}}^R = \frac{1}{B}\sqrt{\sum_{b=1}^{B} \left(W_b - \tilde{W}\right)^2}. \tag{A.3}$$

Given that systematic and random uncertainties are orthogonal, and considering again Eq. (A.1), the composed uncertainty for the averaged width is:

$$u_{\tilde{W}} = \sqrt{\left(u_{\tilde{W}}^S\right)^2 + \left(u_{\tilde{W}}^R\right)^2}. \tag{A.4}$$

In the same manner, the uncertainty of the equivalent radius was propagated as follows:

$$u_{R_{eq}} = \frac{u_\forall}{\left(36\pi\forall^2\right)^{\frac{1}{3}}}. \tag{A.5}$$

And finally, the uncertainty of the dynamic contact angle, ϕ, is Box I: where $m = (y_{nvtl})/(x_{nvtl} - x_{tl})$.

For the forces acting on the bubble, we applied the same procedure for uncertainty propagation. This gives the following equations for uncertainty calculations:

$$u_{F_b} = \left(\rho_l - \rho_g\right)|\mathbf{g}|\, u_\forall; \tag{A.7}$$

$$u_{F_\varsigma} = 2\pi\varsigma\sqrt{\sin^2(\theta)u_{R_d}^2 + R_d^2\cos^2(\theta)u_\theta^2}; \tag{A.8}$$

$$u_{F_{cp}} = \frac{2}{5}\pi\varsigma\sqrt{\left(\frac{2R_d}{R_{eq}}\right)^2 u_{R_d}^2 + \left(\frac{R_d}{R_{eq}}\right)^4 u_{R_{eq}}^2}; \tag{A.9}$$

$$u_{F_R} = \rho_v\sqrt{\left(\frac{dv}{dt}\right)^2 u_\forall^2 + \forall^2 u_{(dv/dt)}^2}; \tag{A.10}$$

$$u_{F_{uy}} = \sqrt{u_{F_b}^2 + u_{F_\sigma}^2 + u_{F_{cp}}^2 + u_{F_R}^2}. \tag{A.11}$$

Appendix B. Methodology validation

For validating the new proposed methodology, we applied it for analyzing the bubbles' images in Fig. 3 from the work of Siedel, Cioulachtjian and Bonjour [16]. We compared our results for the bubble volume temporal evolution with the results from their Fig. 5. We calculated the dimensionless volume and time using the same method employed in [16], for facilitating the results' comparison.

The results are presented in Fig. B.1, where we can see that our procedure is able to capture correctly the shape of the bubble, as well as its characteristics (such as the volume, in this case). The comparison also shows that the uncertainty assumption (about 4 px, as mentioned

$$u_{\phi} = \sqrt{\left[\frac{1}{\left(1+m^2\right)\left(x_{nvtl}-x_{tl}\right)}\right]^2 \left(u^2_{y_{nvtl}} + u^2_{y_{tl}}\right) + \left[\frac{\left(y_{nvtl}\right)}{\left(1+m^2\right)\left(x_{nvtl}-x_{tl}\right)^2}\right]^2 \left(u^2_{x_{nvtl}} + u^2_{x_{tl}}\right)}. \quad \text{(A.6)}$$

Box I.

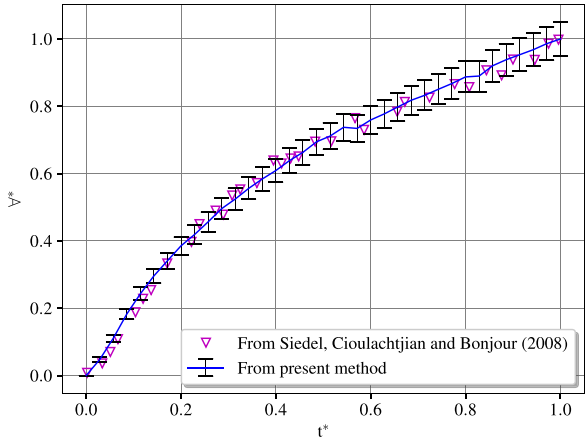

Fig. B.1. Comparison between original volume data from Fig. 5 of Siedel, Cioulachtjian and Bonjour [16] and the results obtained by our method applied to the images in Fig. 3 of [16] work.

in Section 2.2) is also reasonable, as the data from the reference paper remained between the error bar of our measured curve.

In this case, as the authors only provided one cycle of the bubble in their Fig. 3, we were not able to calculate the random uncertainty, both related to ∀ and t. This is the reason why in Fig. B.1 there are no error bars referent to t^* axis. Therefore, the errors in ∀* axis are only due our image-processing procedure (systematic errors from experimental measurement were not included).

Appendix C. Supplementary data

Supplementary material related to this article can be found online at https://doi.org/10.1016/j.expthermflusci.2024.111272.

References

[1] R.F. Gaertner, Photographic study of nucleate pool boiling on a horizontal surface, J. Heat Transfer (1965) 17–29.

[2] B.B. Mikic, W.M. Rohsenow, P. Griffith, On bubble growth rates, Int. J. Heat Mass Transfer 13 (1970) 657–666.

[3] R. Cole, W.M. Rohsenow, Correlations for bubble departure diameters for boiling of saturated liquid, Chem. Eng. Prog. 65 (1969) 211–213.

[4] N. Zuber, M. Tribus, Further remarks on the stabilityof boiling heat transfer. Report 58-5, 1958.

[5] H.J. Ivey, Relationship between bubble frequency, departure diameter, and rise velocity innucleate boiling, Int. J. Heat Mass Transfer 10 (1967) 1023–1040.

[6] A. Suszko, M.S. El-Genk, Saturation boiling of PF-5060 on rough Cu surfaces: Bubbles transient growth, departure diameter and detachment frequency, Int. J. Heat Mass Transfer 91 (2015) 363–373.

[7] A.A. Avdeev, Bubble Systems, Springer Cham, 2016.

[8] G. Giustini, R.I. Issa, Modelling of free bubble growth with interface capturing computational fluid dynamics, Exp. Comput. Multiphase Flow 5 (4) (2023) 357–364, http://dx.doi.org/10.1007/s42757-022-0139-5.

[9] Y. Chen, J. Wang, S. Ouyang, Z. Wang, B. Li, J. Wang, Experimental and LBM simulation study on the effect of bubble merging on saturated pool boiling in pure water, Exp. Comput. Multiphase Flow 6 (2) (2024) 126–134, http://dx.doi.org/10.1007/s42757-023-0174-x.

[10] G. Son, V. Dhir, N. Ramanujapu, Dynamics and heat transfer associated with a single bubble during nucleate boiling on a horizontal surface, J. Heat Transfer 121 (1999) 623–631.

[11] J. Li, Z. Yang, Y. Duan, Experimental study on single bubble growth of R32 + R1234yf binary mixtures during saturated pool boiling, Appl. Therm. Eng. 219 (2023) 119535.

[12] S. Di Bari, A.J. Robinson, Experimental study of gas injected bubble growth from submerged orifices, Exp. Therm Fluid Sci. 44 (2013) 124–137.

[13] Z. Chen, A. Haginiwa, Y. Utaka, Detailed structure of microlayer in nucleate pool boiling for water measured by laser interferometric method, Int. J. Heat Mass Transfer 108 (2017) 1285–1291.

[14] S. Jung, H. Kim, An experimental method to simultaneously measure the dynamics and heat transfer associated with a single bubble during nucleate boiling on a horizontal surface, Int. J. Heat Mass Transfer 73 (2014) 365–375.

[15] G. Huber, S. Tanguy, M. Sagan, C. Colin, Direct numerical simulation of nucleate pool boiling at large microscopic contact angle and moderate Jakob number, Int. J. Heat Mass Transfer 113 (2017) 662–682.

[16] S. Siedel, S. Cioulachtjian, J. Bonjour, Experimental analysis of bubble growth, departure and interactions during pool boiling on artificial nucleation sites, Exp. Therm Fluid Sci. 32 (2008) 1504–1511.

[17] S. Michaie, R. Rullière, J. Bonjour, Experimental study of bubble dynamics of isolated bubbles in water pool boiling at subatmospheric pressures, Exp. Therm Fluid Sci. 87 (2017) 117–128.

[18] M. Mahmoud, T. Karayiannis, Bubble growth models in saturated pool boiling of water on a smooth metallic surface: Assessment and a new recommendation, Int. J. Heat Mass Transfer 208 (2023) 124065, http://dx.doi.org/10.1016/j.ijheatmasstransfer.2023.124065, URL https://www.sciencedirect.com/science/article/pii/S0017931023002181.

[19] M. Mahmoud, T. Karayiannis, Bubble growth on a smooth metallic surface at atmospheric and sub-atmospheric pressure, Int. J. Heat Mass Transfer 209 (2023) 124103, http://dx.doi.org/10.1016/j.ijheatmasstransfer.2023.124103, URL https://www.sciencedirect.com/science/article/pii/S0017931023002569.

[20] E. Dougherty, Mathematical Morphology in Image Processing, first ed., CRC Press, 1992.

[21] A.S. Kornilov, I.V. Safonov, An overview of watershed algorithm implementations in open source libraries, J. Imaging 4 (10) (2018).

[22] J.B. Roerdink, A. Meijster, The watershed transform: Definitions, algorithms and parallelization strategies, Fund. Inform. 41 (2000) 187–228.

[23] J.-B. Kim, H.-J. Kim, Multiresolution-based watersheds for efficient image segmentation, Pattern Recognit. Lett. 24 (1) (2003) 473–488.

[24] Y. He, C. Hu, H. Li, B. Jiang, X. Hu, K. Wang, D. Tang, A flexible image processing technique for measuring bubble parameters based on a neural network, Chem. Eng. J. 429 (2022) 132138.

[25] J.T. Gostick, Versatile and efficient pore network extraction method using marker-based watershed segmentation, Phys. Rev. E 96 (2017) 023307.

[26] A. Hanbury, Image segmentation by region based and watershed algorithms, in: Wiley Encyclopedia of Computer Science and Engineering, John Wiley & Sons, Ltd, 2009, pp. 1543–1552.

[27] P.F. Alvariño, M.L.S. Simón, M. dos Santos Guzella, J.M.A. Paz, J.M.S. Jabardo, L.C. Gómez, Experimental investigation of the CHF of HFE-7100 under pool boiling conditions on differently roughened surfaces, Int. J. Heat Mass Transfer 139 (2019) 269–279.

[28] M.S. Nixon, A.S. Aguado, Feature Extraction and Image Processing, Academic Press, 2002.

[29] N. Otsu, A threshold selection method from gray-level histograms, IEEE Trans. Syst. Man Cybern. 9 (1) (1979) 62–66.

[30] L. Vincent, Morphological transformations of binary images with arbitrary structuring elements, Signal Process. 22 (1) (1991) 3–23.

[31] C. do Amaral, R. Alves, M. da Silva, L. Arruda, L. Dorini, R. Morales, D. Pipa, Image processing techniques for high-speed videometry in horizontal two-phase slug flows, Flow Meas. Instrum. 33 (2013) 257–264.

[32] D. Biolè, M. Wang, V. Bertola, Assessment of direct image processing methods to measure the apparent contact angle of liquid drops, Exp. Therm Fluid Sci. 76 (2016) 296–305.

[33] L.Z. Zeng, J.F. Klausner, R. Mei, A unified model for the prediction of bubble detachment diameters in boiling systems-I. Pool boiling, Int. J. Heat Mass Transfer 36 (9) (1993) 2261–2270.

[34] P.Z. ans Ronghua Huang, S. Huang, Y. Zhang, X. Rao, Experimental investigation on bubble contact diameter and bubble departure diameter in horizontal subcooled flow boiling, Int. J. Heat Mass Transfer 49 (2020) 119105.

[35] M.S. Plesset, S.A. Zwick, The growth of vapor bubble superheated liquids, J. Appl. Phys. 25 (4) (1954) 493–500.

[36] N. Zuber, The dynamics od vapour bubbles in nonuniform temperature fields, Int. J. Heat Mass Transfer 2 (1961) 83–89.
[37] R. Cole, H.L. Shulman, Bubble growth rates at high Jakob numbers, Int. J. Heat Mass Transfer 9 (1966) 1377–1390.
[38] M.G. Cooper, The microlayer and bubble growth in nucleate pool boiling, Int. J. Heat Mass Transfer 12 (1969) 915–933.
[39] W.C. Chen, J.F. Klausner, R. Mei, A simplified model for predicting vapor bubble growth rates in heterogeneous boiling, J. Heat Transfer 117 (4) (1995) 976–980.
[40] J. Du, C. Zhao, H. Bo, A modified model for bubble growth rate and bubble departure diameter in nucleate pool boiling covering a wide range of pressures, Appl. Therm. Eng. 145 (2018) 407–415.